UNIVERSITY OF OKLAHOMA

GRADUATE COLLEGE

DESIGN AND SETUP OF AN ATOM INTERFEROMETER GYROSCOPE USING A STRONTIUM THERMAL BEAM

A THESIS

SUBMITTED TO THE GRADUATE FACULTY

in partial fulfillment of the requirements for the

Degree of

MASTER OF SCIENCE

By

NATHAN MARLIERE
Norman, Oklahoma
2022

DESIGN AND SETUP OF AN ATOM INTERFEROMETER GYROSCOPE USING A STRONTIUM THERMAL BEAM

A THESIS APPROVED FOR THE DEPARTMENT OF ENGINEERING PHYSICS

BY

Dr. Grant Biedermann, Chair

Dr. Michael Santos

Dr. Bin Zheng

Acknowledgments

I will start by extending my thanks and appreciation to my advisor Dr. Grant Biedermann for allowing me to do my master's thesis as a member of his laboratory in the Center for Quantum Research and Technology. This truly has been a better experience than what I could have had ever hoped for.

I would also like to thank my other thesis committee members, Dr. Michael Santos and Dr. Zheng Bin, for their consideration of my thesis and the advice they have provided me along the way. I am grateful for the teachings they have provided me during these past 17 months.

Additionally, this thesis would not have been possible without the generous support from the company Intelligent Fiber Optic Systems (IFOS).

I am also deeply thankful for Luke Kraft and Akbar Jahangiri Jozani, without whom none of this would have been possible. He has helped me hugely in the realization of this thesis but also regarding research in general, as it was something totally new for me.

I would also like to thank my teachers and the administration at Polytech Clermont-Ferrand in France for helping me apply for the dual degree that allowed me to come to the University of Oklahoma.

My greatest thanks go out to my parents, my family, and my friends for supporting me every step of the way as I was navigating graduate college in a foreign country.

Thank you,

Nathan Marliere

Abstract and Keywords

A gyroscope was developed and demonstrated using strontium atom interferometry on a rotating platform. This will allow us to study the interplay of the Atomic Interferometer Gyroscope (AIG) physics with large rotation rates. This apparatus, not tested yet, is very promising because the proof-of-concept experiment for the new strontium interferometer used by the gyroscope gave us good results and there are many improvements to be explored such as Large Momentum Transfer (LMT). The applications for this apparatus can be inertial navigation and geophysical studies. The principle of operation is as follows: A thermal strontium atomic beam crosses three laser interaction regions where resonant beams stimulate transitions between strontium ground states and excited states. With this transition, these beams transfer momentum to atoms that divide, deflect and recombine the atomic wavepackets. A rotation induced phase shift between the two arms of the gyroscope causes a change in the detected number of atoms with a particular internal state. The rotations phase shifts are proportional to the vector velocity of the atoms. Furthermore, rotation Doppler-shifts the π and ${}^{\pi}/_{2}$ beams.

Keywords: Atomic Interferometer gyroscope, Rotation measurements, Atom interferometry, Strontium transitions, Laser experiment

Table of Contents

Table of Figures

Table of Tables

CHAPTER 1 - Introduction

1.1 Presentation of gyroscopes

A gyroscope is a device that can measure the angular velocity (ω in Radians/second) relative to an inertial reference frame. Integrating this angular velocity provides orientation and position information (if an initial orientation or position is provided). This paper describes a gyroscope based on Atom Interferometry. Its high-precision measurement makes it a state-of-the-art gyroscope. A gyroscope measures the rotation information along three different axes but only one at a time. Thus, it can track the twists, turns, and rolls of a moving object. Therefore, this access to orientation information has many applications, mainly based on navigation and geophysics sensing[1]. We will discuss these applications later in this chapter. There are two principal types of gyroscopes: mechanical gyroscopes based on inertia and resonance effects and optical (or Interferometric) devices using the Sagnac effect.

The main issues for all types of gyroscopes are the errors in measuring the angular velocity. These errors come in two basic types: deterministic and random. The main deterministic errors are the scale factor and the bias. The scale factor can be expressed as follows: suppose a gyroscope reads the rates of 1.1 and 4.4 radians per second when rotating at 1 and 4, respectively. The ratio between the reading value and the actual value is the scale factor, here 1.1. The bias is a non-zero result when the gyroscope is not rotating. The main random error is the “Random Walk”. It describes the average deviation or error in your rate signal. For example, suppose that the gyroscope is rotating at 1 radian per second. But, because it isn't perfect, it might measure 1.1 or 0.9 radians per second. This error happens independently from the deterministic errors.

1.1.1 Mechanical gyroscopes

The experiment of the French scientist Leon Foucault in the mid-19th century was first realized to observe the rotation of the Earth. This experiment consisted of a very long and heavy pendulum that was established to swing back and forth on the north-south plane with the Earth turning beneath it. Foucault decided to corroborate this experiment in another way: he put a high-speed rotating wheel on a ring. This ring supported the wheel in a way that the spinning axis of the wheel could move independently. The result of this experiment was the ring moving over the day period because it was connected to the Earth’s rotating surface. The wheel’s rotating axis pointing in the original direction during the experiment was proof that the Earth is rotating in a twenty-four-hours period. Observing the Earth’s rotation was the first motivation for the gyroscope.

A mechanical gyroscope can be defined as any rotating object subject to two intrinsic properties: the gyroscopic effect and the precession. All the rotating bodies exhibit these properties, including massive objects like the Earth or the Sun. Gyroscopic inertia can be described as rigidity in the space of the spin axis. This property comes from Newton's first law of motion, which explains that an object tends to remain in its state (rest or motion) unless external forces perturb the initial state. Thus, a free-rotating wheel of a gyroscope tends to keep rotating along the same axis and in the same plane unless a new perturbation modifies the axis of rotation. An excellent example of this property is the rifle. All the guns make the bullets rotate because due to the gyroscopic inertia, a rotating bullet will try to maintain its spinning axis in flight as a straight line than it wouldn't if it was not rotating.

The precession happens when a force is applied to a gyroscope. This force produces a change in the direction of the axis of rotation. As a result, the axis will move perpendicular to the direction in which the force is applied. The angular momentum of the rotating wheel and the applied force produce the motion of the axis. The three axes of a gyroscope are called the spin, torque, and precession axis. The spin axis is the axis that the wheel is rotating. The applied force will cause the spin axis to move into the torque axis, rotating the gimbal about the precession axis[1]–[3].

Let's take an example of a two-free axis gyroscope; the simplified equations governing the physical phenomenon are:

$$C_y = -I\Omega\omega_z \tag{1.1}$$

$$C_z = I\Omega\omega_y \tag{1.2}$$

Where C_y and C_z are the torques created along the y and z-axis, respectively. I is the moment of inertia of the spinning wheel; Ω is the angular velocity of the spinning wheel along its rotation axis; and ω_y and ω_z are the precession speeds along the y and z-axis, respectively. We can see from. The equations (1.1) and (1.2), the output torque is proportional to the rotational speed of the spinning wheel due to the imposed precession motion[1].

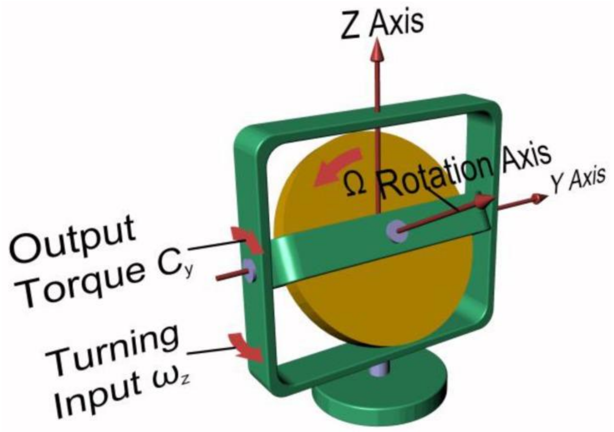

Figure 1-1. Torque acting on a two-axis free moving gyroscope. Figure reproduced from [1].

1.1.2 Sagnac effect gyroscopes

The principle of optical gyroscopes relies on the difference in propagation times between two beams propagating in opposite directions in a closed or open optical path. The rotation of the device containing the optical path will induce a change in the path length which finally generates a phase difference between the two light beams. The Sagnac effect consists of this rotation-induced phase difference which is the basic principle of all interferometer-based gyroscopes (light or atomic).

George Marc Sagnac first discovered this effect in 1913 by combining the results of Michelson-Morley's study on Earth's rotation dynamics and his observations of electromagnetic waves in non-inertial reference systems. The Sagnac principle is a derivation of the general relativity theory. It states that a relative phase shift can be observed between two counter-propagating light beams in a rotating ring structure. Thus, the phase change can be related to the angular speed of the ring. Because of the high speed of the light, the phase shift between the two counter-propagating beams was too small, and so, at this time, no devices were genuinely realizable.

In 1966, The scientist Schultz-Du Bois invented the first device based on the Sagnac effect. This device was the ring laser gyroscope. It was a cylindrical mirror in which the light followed a circular path. The principle was the following: two counter-rotating light beams with the same wavelength were introduced into the cylinder. These two beams interacted with each other by creating interferences, producing a permanent stationary wave with respect to an external reference system. The new standing wave created comprised nodes and anti-nodes whether the device was standing or rotating. During the apparatus rotation, a detector counted the nodes and anti-nodes to evaluate the angular velocity of the ring.

Indeed, the number of nodes is proportional to the ring's length and inversely proportional to the wavelength. Knowing the number of nodes in the time unit makes it possible to determine the ring velocity.

Let's now calculate the phase shift of basic rotational optical sensors[4], [5]. As Explained before, these devices generate a difference in the optical path ΔL between two counterpropagating beams proportional to the angular velocity Ω.

Consider a disk with radius R rotating at an angular speed Ω on an axis perpendicular to the disk plane. This rotating disk is represented in Figure 1-2. Two identical photons propagate in clockwise and counterclockwise directions around the disk. If the angular velocity is null, the beam will travel at the speed of light in air c, arriving at the starting point 1 at time $t = \frac{2\pi R}{c}$ with a trip length of $2\pi R$.

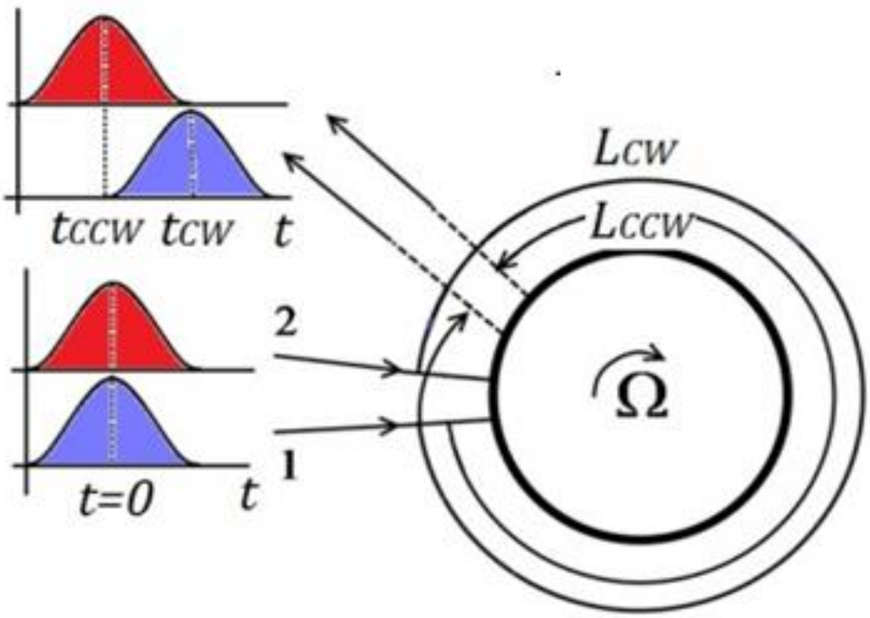

Figure 1-2. Sagnac effect principle in a circular closed loop. Figure reproduced from [1].

Now, the disk is rotating Clockwise (CW). The rotation induces two different optical paths for the clockwise and counterclockwise (CCW) optical beams, L_{CW} and L_{CCW}, respectively. So, the photons that now propagate counterclockwise will arrive at point 2. Due to the rotation, L_{CCW} will be shorter than $2\pi R$:

$$L_{CCW} = 2\pi R - R\Omega t_{CCW} = c \times t_{CCW} \tag{1.3}$$

Here, $R\Omega$ is the tangential angular speed of the device and t_{CCW} is the time taken by the photon to cover the distance L_{CCW}. The clockwise propagating photon will also arrive at point two, covering a longer distance than $2\pi R$ due to the ring rotation. So, we can express L_{CW} as:

$$L_{CW} = 2\pi R - R\Omega t_{CW} = c \times t_{CW} \tag{1.4}$$

Using (1.3) and (1.4), we can express the two times taken by each type of photons to cover their distance in the ring, respectively t_{CCW} and t_{CW}:

$$\begin{cases} t_{CCW} = \frac{2\pi R}{c+R\Omega} & (1.5) \\ t_{CW} = \frac{2\pi R}{c-R\Omega} & (1.6) \end{cases}$$

Using (1.5) and (1.6), we can express the time difference :

$$\Delta t = t_{CW} - t_{CCW} = \frac{4\pi R^2 \Omega}{c^2 - R^2 \Omega^2} \quad (1.7)$$

For $R\Omega = \mathrm{v} \ll \mathrm{c}$, we can simplify the equation (1.7) as:

$$\Delta t \approx \frac{4\pi R^2 \Omega}{c^2} = \frac{4A\Omega}{c^2} \quad (1.8)$$

Where A is the area of the disk. So, the phase shift can be expressed as:

$$\Delta\Phi \approx \frac{2\pi \Delta \mathrm{t}}{\frac{\lambda}{c}} = \frac{8\pi A\Omega}{\lambda c} \quad (1.9)$$

We can now compare the optical gyroscope to the Atomic Interferometer Gyroscope (AIG). An atom has the same property as a photon, it can be a particle or a wave. So, an atomic interferometer can be subject to the Sagnac effect and then, works as a gyroscope. Figure 1-3 shows that many atoms must be prepared before entering the loop. Indeed, they must be concentrated in phase space and selected in specific atomic states. Then, coherent sources of light (laser beams) will manipulate the atoms to split and reflect them into a coherent superposition of momentum state. The manipulation aims to form a closed loop. Finally, a laser is used to measure the phase shift of the recombined atoms during the rotation of the AIG.

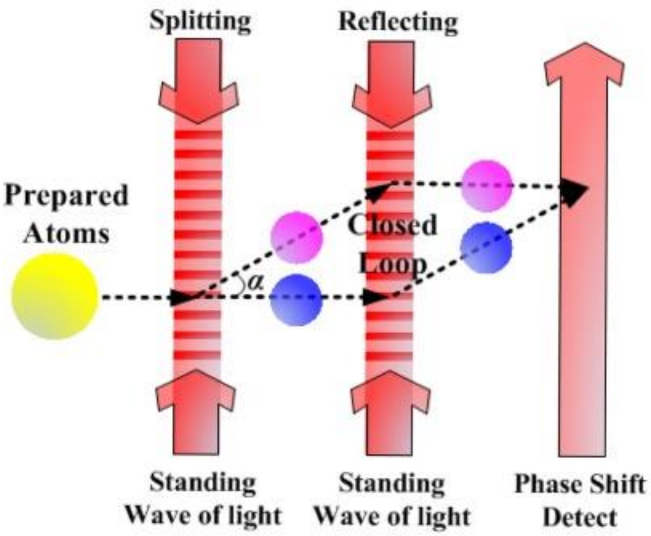

Figure 1-3. Basic principle of an Atom Interferometer Gyroscope. Figure reproduced from [6].

We already know the Phase shift induced by the rotation of a ring in an optical gyroscope:

$$\Delta\Phi \approx \frac{8\pi A\Omega}{\lambda c} \tag{1.10}$$

In addition, we can express the phase shift of an AIG (see [6]) as:

$$\Delta\Phi \approx \frac{8\pi m A\Omega}{h} \tag{1.11}$$

Where m is the atom's mass and h is the plank constant. Then, we can compare the sensitivity between AIG and optical gyroscope; we have:

$$\frac{\Delta\Phi_{AIG}}{\Delta\Phi_{Light}} = \frac{m\lambda c}{h} > 10^{10} \tag{1.12}$$

We can conclude that an AIG is more sensitive to rotation by a factor of 10^{10} compared to optical gyroscope if they have the same closed loop area. However experimentally, compared with optical gyroscopes, the AIG is far from the sensitivity found in theory. It is mainly due to the enclosed loop area, which is smaller by many orders. In fact, it is difficult to manipulate the atoms in a the closed loop as big as the optical gyroscope does.

1.2 History of Laser manipulation of Atoms

To be viable, atom interferometry requires a bright source of neutral atoms and technics to manipulate the atoms precisely. These technics can be analogous to light manipulation with optical elements. During the last decades, these technics, such as laser cooling, trapping, and atomic manipulation have been improved to obtain a better source of atoms. A brief and relevant history of these developments follows.

1.2.1 Laser Cooling

The 1970s and 80s were important decades in which scientists discovered how to cool atom beams just above absolute zero. The first cooling realized during these years was ion beams cooling (below 40 kelvin) in 1978. Here is the principle used: When the ions are in rest states, they can absorb photons at the resonance frequency, but when these are moving toward the beam, they experience a Doppler shifting that lower their frequency. So, the photons used were detuned in the red frequency to have the exact resonance frequency while moving to the beam. These absorbed and reemitted photons reduced the ions' energy and so, their speed until other types of heating balanced the cooling.

The next significant advance in laser cooling was in 1982. Philips and Harold Metcalf published a paper on cooling neutral atoms. This technique used Doppler cooling, but they also used a slowly changing magnetic field during the deceleration so the cooling could be maintained over a long distance. The device used is now known as Zeeman slower.

In the late 1980s, physicists determined theoretically the lowest possible temperature allowed by Doppler cooling for sodium atoms: 240 mK. But this limit was shattered accidentally by Phillips's group in 1988 thanks to a technic developed by Steven Chu in 1985. They could cool their atoms to about 43 microkelvins. Indeed, the first Doppler limit theory did not consider the effect of the laser beams' polarization and more. With a better understanding of laser cooling, scientists could achieve sub-doppler cooling in 1995. For their work on laser cooling, Phillips and Chu won the Nobel Prize in 1997.[7]

1.2.2 Atom Interferometry

In 1924, the physicist Louis De Broglie used the work of Einstein on photons to demonstrate the wave-particle duality of material particles such as atoms or neutrons. This theory relates the wavelength of a particle to its momentum: lambda = h/p. Two main experiments rapidly demonstrated this theory:

- Davisson and Germer observed the diffraction of electrons on a metallic crystal lattice surface in 1927
- In 1930, the scientists Estermann and stern realized the diffraction of a helium atom beam on a NaCl crystal. This experiment has been used to observe neutron diffraction.

These experiments have opened the possibilities of mater-wave interferometers, but at this time, there were two main problems to solve:

- The first one was the wavelength of the matter waves. Indeed, most of the wavelengths are smaller than a nanometer. For example, lithium atoms with a velocity of 1000m/s have a wavelength of 54 pm. This value is more than ten thousand times smaller than the light wavelength.
- The second problem is the non-existence of natural matter-wave optical elements such as beamsplitters or mirrors. It is due to the high chance of having inelastic reflections on solid surfaces. Moreover, elastic reflections on solids are frequently non-coherent because the surface roughness is much larger than the wavelength.

In 1952, Marton's lab scientists built the first Mach Zehnder electron interferometer. It used electron diffraction on thin metallic crystals. But, because of electrons' sensitivity to electric fields, this type of interferometer did not develop too much. In the same way, neutron interferometers were developed during this period using successive Bragg reflections on three gratings. Hence, they were called "Perfect crystal Neutron Interferometers". The problem with these interferometers was the relative insensibility of neutrons to electric fields and that they interact weakly with the matter.

During Rabi's and N.F. Ramsey's experiments, the scientists discovered that the internal states of the atoms could play the role of the photon polarization states. With this discovery, the First experiments on atom interferometry started in 1991 and were already very precise:

- O. Carnal and J. Mlynek worked on a Young double-slit experiment using an atomic beam of helium
- D. Pritchard realized a new Mach-Zehnder Interferometer using a sodium atomic beam.
- J. Helmcke built an interferometer based on Ramsey fringes in saturated absorption. This apparatus first showed the Sagnac effect for atomic waves.
- M. Kasevich and S. Chu also created a Mach Zehnder interferometer using cold sodium atoms and laser diffraction. This interferometer has been used to measure the local acceleration of gravity with an unprecedent precision.

This research field has developed rapidly since 1991, and most interferometers were based on Mach Zehnder structure[8].

1.3 Motivation

1.3.1 Inertial navigation

The inertial navigation system comprises three accelerometers and three gyroscopes. These inertial sensors and a computer can compute the position, attitude, and velocity. Furthermore, this system uses the dead reckoning (DR) principle. Indeed, in inertial systems, the precedent information of a vehicle’s position and the accelerations and angular rotations measured by the sensors allows to determine its current position. The position variation and the velocity of the moving object comes from one or two acceleration integrations: one for the velocity and two for the position. With initial conditions, these variations give the current position and velocity. The angular rates provide the attitude of the moving object along three axes and transform navigations information from the body frame to the reference frame[9], [10].

In addition, the platform on which the sensors are mounted is linked to gimbals such that the platform always remains aligned with the navigation frame. Indeed, The gimbals are connected to torque motors, so when a gyroscope senses a rotation on an axis, the motors rotate the platform in response.

Thus, the output of the accelerometers is directly integrated for velocity and position in the navigation frame. This system was efficient at the beginning of inertial navigation, but nowadays, computers can simulate the rotations thanks to software. This system, named strapdown, is now favored for many reasons, such as reliability and low power usage. The figure below summarizes the basic principle of inertial navigation.

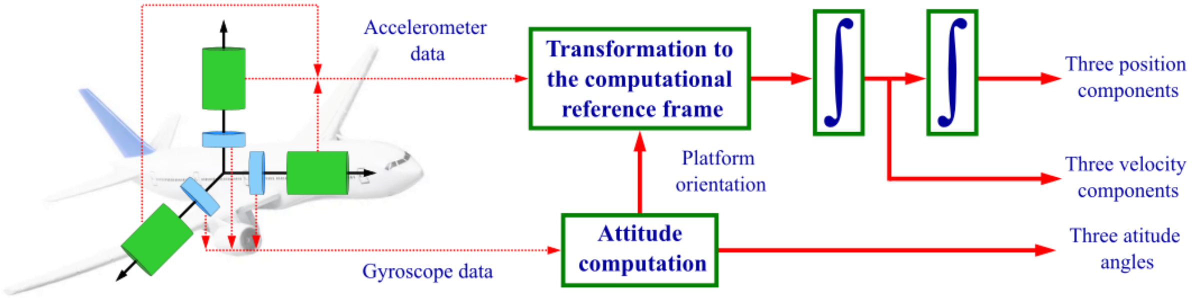

Figure 1-4. Principle of inertial navigation

Numerous objects and systems nowadays use this system to compute their position. These include aircraft (for attitude control, flying during poor visibility conditions), submarines (external references may be dangerous during covert operations), rockets, and autonomous vehicles. Nowadays, these objects require compact and reliable systems. Atom Interferometer gyroscopes meet more and more of these expectations as they are improved. Additionally, cost and size have been significantly improved these last years.

Moreover, this system is sometimes safer and more reliable than Global Positioning Systems (GPS). Indeed, GPS requires the exchange of data between satellites and moving objects. This "communication" with a satellite can be intercepted by an opponent in military cases or disturbed by elements such as water, rocks, or trees. So inertial navigation is essential as a complement or alternative to the GPS[10].

Even if the inertial navigation system is essential nowadays, this type of system is subject to critical errors due to the DR principle. Indeed, if a suitable position accuracy is wanted over a long time, high-accuracy gyroscopes and accelerometers are needed. For instance, an accelerometer with a bias error of Δa leads to a position error of $\frac{1}{2}\Delta a T^2$ due to the double integration. On the gyroscope part, offset angle measurement is $\Delta\theta$ leads to the position error $\Delta\theta vT$ and so, using the rate bias error $\Delta\Omega = \frac{\Delta\theta}{T}$ the position error is approximatively $\Delta\Omega vT^2$.

1.3.2 Geophysics

1.3.2.1 Earth rotation variation measurements

During the last two centuries, scientists discovered that the Earth's rotation and the Length-Of-Day (LOD) are not constant. These changes can be observable from sub-daily to decadal and longer times scale. A wide diversity of processes are causing the variations in Earth's angular momentum, such as external tidal forces, internal processes between the crust and the fluid core, and fluid movements involving oceans and the atmosphere.

The most important mechanism responsible for the fluctuation of the rotation rate is the oceanic tidal angular momentum. When we talk of oceanic tides, we refer to a moving mass of water with a velocity and direction. Both the moon and the Sun exert gravitational forces on Earth's waters that generate two bulges in the Earth's oceans. Due to the moon's proximity, the two bulges mainly depend on its gravitational forces: one closest to the moon and one on the opposite side of the globe. The bulges result in tides that affect the Earth's rotation rate. Indeed, the bulges lag slightly and so apply a torque on the Earth's angular momentum.

The very long baseline interferometry (VLBI) technique precisely measures the Earth's angular momentum change[11], [12]. This method compares signals from a reliable and distant source, such as quasar, with two highly spaced antennas. As the Earth rotates, the baseline distances between antennas can be recovered, along with the orientation of those baselines in space (precession, nutation, and Earth rotation). The VLBI's accuracy is about 10 μs for the Length of Day (LOD) measurement and 0.5 nrad for the pole position measurement. However, this method requires considerable effort. So, it is worthwhile to explore complementary methods for accurately estimating Earth’s rotation and polar motion. The requirements for geodesy can be summarized as follows:

- Sensitivity to angular motion of <0.1 prad/s over an integration time of about 1 h
- Sensor stability of 1 part in 10^9 over several months (a requirement for annual wobble’s measurement)
- Resolution for the sensor orientation of ~1 nrad (in 1 h), corresponding to a polar motion effect of around 1 cm at the pole

These requirements can be fulfilled requirements can be satisfied by Sagnac-effect gyroscopes [11], [13], [14]. Therefore, Atomic Interferometer Gyroscopes are an excellent alternative to the VLBI technique.

1.3.2.2 Seismic Wave Studies

As explained before, the Sagnac effect gyroscopes are suitable for precisely measuring Earth's rotation rate. However, the rotational signal caused by an earthquake is stronger than these small perturbations of Earth's rotation. Moreover, the range of angular velocities to be measured is wide and the required bandwidth is between 3mHz and 10Hz. Only ring laser gyroscopes are currently involved in seismological applications[15]. Unlike seismometers, the Sagnac effect gyroscopes are not based on mass inertia. Therefore, they have no moving mechanical parts. It's an advantage because no restitution process is required to analyze the ground motion. Typical seismic signals need high sensor stability for up to one hour of continuous data acquisition.

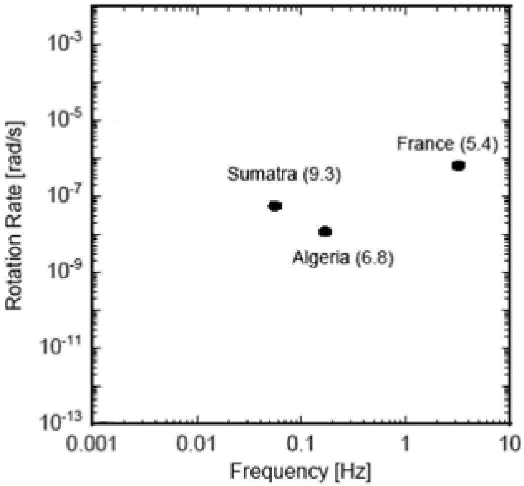

Figure 1-5. Observed signal strength of some earthquakes at different epicentral distances. Figure reproduced from [15].

Figure 1-5 illustrates some essential characteristics for detecting rotations from seismic signals. The diagram shows most of the measurement range of interest for seismic studies. The relevant frequency window is plotted horizontally, while the magnitude of the respective rotation rates is displayed vertically. According to this figure, optimized Sagnac-effect gyroscopes may be in the earthquake magnitude's range of measurements.

1.4 Overview of the thesis

Chapter 2 reviews the principal methods of manipulating atoms with lasers used in this experiment. This includes techniques used for transverse cooling of the atomic beam, detection, and π and $\pi/2$ beams transitions used to construct the interferometer. Moreover, this chapter will cover the atom interferometry theory by outlining the calculation and interpretation of the Sagnac phase shift and presenting a theoretical model of the gyroscope signal for our experiment. Chapter 3 contains a detailed description of the experimental apparatus. Chapter 4 provides a proof of concept of the interferometer for our gyroscope. Finally, chapter 5 summarizes the current status of the experiment and discusses the outlook for the future.

CHAPTER 2 - Theoretical background

2.1 Laser manipulation of atoms

This section will expose the most relevant principles of laser manipulation of atoms and laser colling used in the experiment. In addition, this section will give an abridged treatment of these theories by summarizing the essential results of the complete derivation theories you can find in the cited references.

2.1.1 ^{88}Sr atom transitions

The atom we use for this experiment is the ^{88}Sr. This atom is part of the alkaline-earth-metal atom family. The interest in these atoms for precision interferometry has increased during the last decade because of their unique characteristics. One of their features is related to their ground state. Indeed, the $^1S_0$ ground state has zero angular momentum, and because bosonic atoms such as the ^{88}Sr do not even have a nuclear spin, their ground state has zero magnetic moments. This leads to ground-state ^{88}Sr being extremely insensitive to external magnetic fields. Another characteristic of alkali-earth-like atoms is their two-valence-electron structure. The-two-valence-electrons energy levels can form singlet (S = 0) or triplet (S = 1) states. We will discuss the importance of this characteristic later in this section. The last important feature is the absence of a hyperfine structure in the ground state. The consequence is that Raman transitions are not available for ^{88}Sr; instead, Bragg diffraction will still be employed to control the atomic momentum coherently[16]–[18].

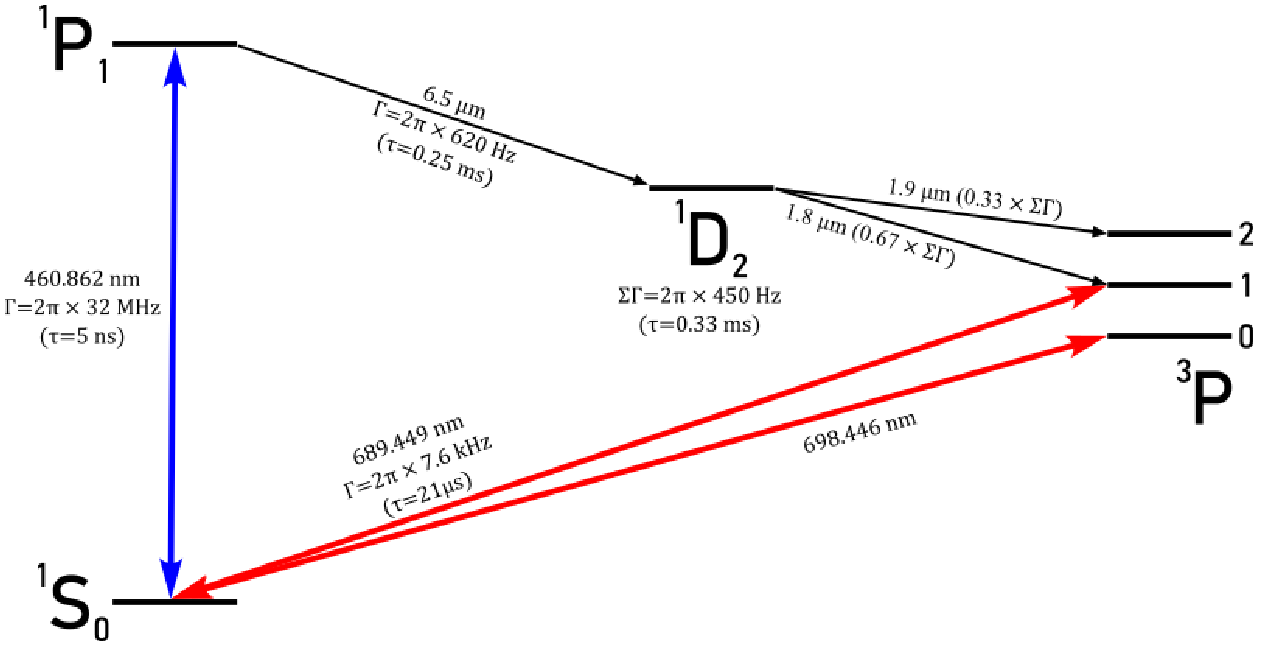

Figure 2-1. Incomplete strontium atomic transitions diagram

We can now discuss the transitions used for the experiment. As explained above, all these transitions are two-level system transitions. The first transition used for this experiment is the $^1S_0$ → $^1P_1$ transition. This transition is a classical electric dipole transition allowed by the selection rules. It is strongly coupled with a linewidth of 32MHz to a light held with a wavelength of 460.862 nm. This transition is used for the detection and the Doppler cooling we will see in the following sections. The second transition used in this experiment is the $^1S_0$ → $^3P_1$ transition. It shouldn't exist because the spin selection rules forbid this transition. However, this type of transition can be allowed because the LS-Coupling scheme doesn't sufficiently describe the behavior of heavy atoms. This difficulty in describing LS coupling for heavy atoms is named LS-coupling breakdown. The spin-orbit and other relativistic effects induce the mixing of states with the same total angular momentum J and different spin S. In the case of Sr, the small amount of S = 0 $^1P_1$ state mixes into the $^3P_1$ state. It then allows the S = 1 transition to support dipole transitions. Such transitions are characterized by narrow linewidths and rather long lifetimes. For strontium, the $^1S_0$ → $^3P_1$ triplet transition is highly favorable with a 7.6 kHz linewidth[19]–[21].

2.1.2 Two-level atom

To describe the concept of Rabi oscillations and ac Stark shifts, we have to consider our system as a two-level atom system interacting with radiation. In this section, we will use a semiclassical treatment. For more information, see [22], [23]. The radiation is treated as a classical electric field, but we use quantum mechanics to treat the atom.

Let's set up the equations for this system. First, we can start with the time-dependent Schrodinger equation:

$$i\hbar \frac{\partial \Psi}{\partial t} = H\Psi \tag{2.1}$$

In our case, the Hamiltonian has two parts. $H_I(t)$ describes the interaction between the atom and the electric field that perturbs the eigenfunctions of H_0. This part is time-dependent. The unperturbed eigenvalues and eigenfunctions of H_0 are just the atomic energy levels and wavefunctions.

$$H = H_0 + H_I(t) \tag{2.2}$$

In the case of a two-level system, the spatial wavefunctions must satisfy the following:

$$\begin{cases} H_0\psi_1(r) = E_1\psi_1(r) \\ H_0\psi_2(r) = E_2\psi_2(r) \end{cases} \tag{2.3}$$

These atomic wavefunctions are not stationary states of the full Hamiltonian, $H_0 + H_I(t)$, but the wavefunction at any instant of time can be expressed in terms of them as follows:

$$\Psi(r,t) = c_1(t)\psi_1(r)e^{-iE_1t/\hbar} + c_2(t)\psi_2(r)e^{-iE_2t/\hbar} \tag{2.4}$$

We can now introduce the perturbating oscillating electric field $E = E_0 \, cos\,(\omega t)$. This electromagnetic radiation produces a perturbation described by the Hamiltonian

$$H_I(t) = e\boldsymbol{r} \cdot \boldsymbol{E}_0 cos(\omega t) \tag{2.6}$$

$e\boldsymbol{r}$ corresponds to the electric dipole, where r is the electron's position with respect to the atom's center of mass. So $H_I(t)$ describe the energy of an electric dipole in an electric field. The interaction with the radiation mixes the two states with energies E1 and E2. Putting the equation 2.4 into the Schrodinger equation 2.1 leads to the following system

$$\begin{cases} i\dot{c_1} = \Omega cos(\omega t) e^{-i\omega_0 t} c_2 \\ i\dot{c_2} = \Omega^* cos(\omega t) e^{i\omega_0 t} c_1 \end{cases} \tag{2.7}$$

Where $\omega_0 = (E_1 - E_2)$ and the Rabi frequency Ω is defined by

$$\Omega = \frac{\langle 1 | e\boldsymbol{r} \cdot \boldsymbol{E}_0 | 2 \rangle}{\hbar} = \frac{e}{\hbar} \int \psi_1^*(r) \boldsymbol{r} \cdot \boldsymbol{E}_0 \, \psi_2(r) \, d^3r \tag{2.8}$$

To find a solution to the interaction between the atom and a monochromatic radiation, we can write system 2.7 as

$$\begin{cases} i\dot{c_1} = \frac{\Omega}{2} \left\{ e^{i(\omega - \omega_0)t} + e^{-i(\omega + \omega_0)t} \right\} c_2 \\ i\dot{c_2} = \frac{\Omega}{2} \left\{ e^{i(\omega - \omega_0)t} + e^{-i(\omega + \omega_0)t} \right\} c_1 \end{cases} \tag{2.9}$$

Because the term with $(\omega + \omega_0)t$ oscillates very fast, it averages to zero over any reasonable interaction time, so we obtain:

$$\begin{cases} i\dot{c_1} = \frac{\Omega}{2} e^{i(\omega - \omega_0)t} c_2 \\ i\dot{c_2} = \frac{\Omega^*}{2} e^{-i(\omega - \omega_0)t} c_1 \end{cases} \tag{2.10}$$

Solving this system for c_2 leads to

$$\frac{d^2c_2}{dt^2} + i(\omega - \omega_0)\frac{dc_2}{dt} + \left|\frac{\Omega}{2}\right|^2 c_2 = 0 \tag{2.11}$$

So, the probability of being in the upper state is obtained by solving equation 2.11 with the initial conditions $c_1(0) = 1$ and $c_2(0) = 0$, we find:

$$|c_2(t)|^2 = \frac{\Omega^2}{W^2} sin^2\left(\frac{Wt}{2}\right) \tag{2.12}$$

With $W^2 = \Omega^2 + (\omega - \omega_0)^2$. Finally, at resonance, we have $\omega = \omega_0$, so the probability for an atom to be in the state $|2\rangle$. After applying the light field for a time t, the population of atoms in the excited state is given by

$$P_e = |c_2(t)|^2 = sin^2\left(\frac{\Omega t}{2}\right) \tag{2.13}$$

We can now discuss the a.c. Stark effect. This effect arises from the fact that the perturbing radiation also changes the energy of the levels. You can find the complete derivation of the a.c. Stark effect in [22]. The result of this derivation shows that the states are shifted from their unperturbed eigenfrequencies by

$$\Delta\omega_{light} = \frac{\Omega^2}{4\delta} \tag{2.14}$$

2.1.3 Laser cooling

In the previous section, we have seen the interaction between radiation and a two-level atom initially at rest. The radiative force can also change the velocity distribution of an ensemble of moving atoms. The interaction with a laser beam can modify both mean velocity $\langle v\rangle$and the velocity dispersion Δv around the mean value. It can reduce or increase $\langle v\rangle$, an effect called slowing down or acceleration. It can also reduce or increase the velocity spread Δv, which characterizes the disordered motion of the atoms. The decrease of Δv induced by the interaction with laser light is called “laser cooling”. This chapter describes the laser cooling mechanism in the simple case of two-level atoms. In order to change Δv, the radiative force must depend on v. A force independent of v would just translate the whole velocity distribution without changing its shape. The simplest way to introduce a velocity dependence in the radiative force exerted by a laser beam with frequency ω on atoms with frequency ω_0 is to use the Doppler effect, which changes the detuning $\delta = \omega - \omega_0$ from resonance by an amount proportional to the velocity v of the atom. Since the radiative force depends on the detuning δ, the velocity dependence of the detuning induces a velocity dependence of the force[23].

The scattering force for a two-level atom is easily understood as the photon momentum $\hbar\boldsymbol{k}$ times the scattering rate ΓP_e. Here, Γ is the transition rate Γ = 1/τ, and the excited-state population P_e can be found from the solution of the optical Bloch equations[24]. The scattering rate using the Bloch optical equations is

$$R_{scatt} = \Gamma P_e = \frac{\Gamma}{2}\left(\frac{\frac{\Omega^2}{2}}{\delta^2+\frac{\Omega^2}{2}+\frac{\Gamma^2}{4}}\right) \tag{2.15}$$

Which leads to the scattering force

$$\boldsymbol{F} = \hbar\boldsymbol{k}R_{scatt} = \frac{\hbar\boldsymbol{k}\Gamma}{2}\left(\frac{\frac{\Omega^2}{2}}{\delta^2+\frac{\Omega^2}{2}+\frac{\Gamma^2}{4}}\right) \tag{2.16}$$

Here $\delta = \omega - \omega_0$ is the laser frequency detuning from the atomic resonance ω_0 and the Rabi frequency characterizes the strength of the atom-laser interaction. It is often convenient to express the scattering force in terms of the saturation parameter, s:

$$\boldsymbol{F} = \frac{\hbar\boldsymbol{k\Gamma}}{\boldsymbol{2}}\left(\frac{\boldsymbol{s}}{\boldsymbol{1+s}}\right) \tag{2.17}$$

Where s is a measure of how hard the optical field drives the atomic transition for a given laser detuning:

$$\boldsymbol{s} = \frac{\frac{\Omega^2}{2}}{\delta^2 + \frac{\Gamma^2}{4}} = \frac{s_0}{1 + \left(\frac{2\delta}{\Gamma}\right)^2} \tag{2.18}$$

$$\boldsymbol{s_0} = \frac{2\Omega^2}{\Gamma^2} = \frac{I}{I_{sat}} \tag{2.19}$$

Here $I_{sat} = \frac{hc\pi}{3\tau\lambda^3}$ is the saturation intensity.

Table 2-1. summarizes the different parameters we use in our experiment for the possible cooling transition $^1S_0 \rightarrow {}^1P_1$[25].

Transition	$\left(\Gamma/_{2\pi}\right)$	λ (nm)	I_{sat}
$^1S_0 \rightarrow {}^1P_1$	30.5 MHz	461	40.7 mW/cm^3

Table 2-1. Important parameters of the 1S0→1P1 strontium atomic transition

At high intensities ($s_0 \gg 1$, or the intensity $I \gg Isat$), the atomic populations in the ground and the excited states equalize, such that the maximum excited state population $P_e = 1/_2$, and the scattering force saturate at the maximum value

$$\boldsymbol{F_{max}} = \hbar \boldsymbol{k} \frac{\Gamma}{2} \tag{2.20}$$

Equivalently, and again using the relation $\frac{I}{I_{sat}} = \frac{2\Omega^2}{\Gamma^2}$, we can express the scattering force as

$$\boldsymbol{F} = \frac{\hbar k\Gamma}{2}\left(\frac{\frac{I}{I_{sat}}}{1 + \frac{I}{I_{sat}} + \frac{4\delta^2}{\Gamma^2}}\right) = \frac{\hbar k\Gamma}{2}\left(\frac{I}{I + I_{sat}}\right)\frac{\left(\frac{\Gamma}{2}\sqrt{1 + {}^{I}/_{I_{sat}}}\right)^2}{\delta^2 + \left(\frac{\Gamma}{2}\sqrt{1 + {}^{I}/_{I_{sat}}}\right)^2} \tag{2.21}$$

The scattering force as a function of laser detuning for three intensities is plotted in Figure 2-2. The increased width with increasing intensity is a result of power broadening of the transition lineshape. At high intensities, the absorption exactly on resonance does not increase above the minimum necessary to equalize the populations in the ground and excited states, but the absorption in the wings increases.

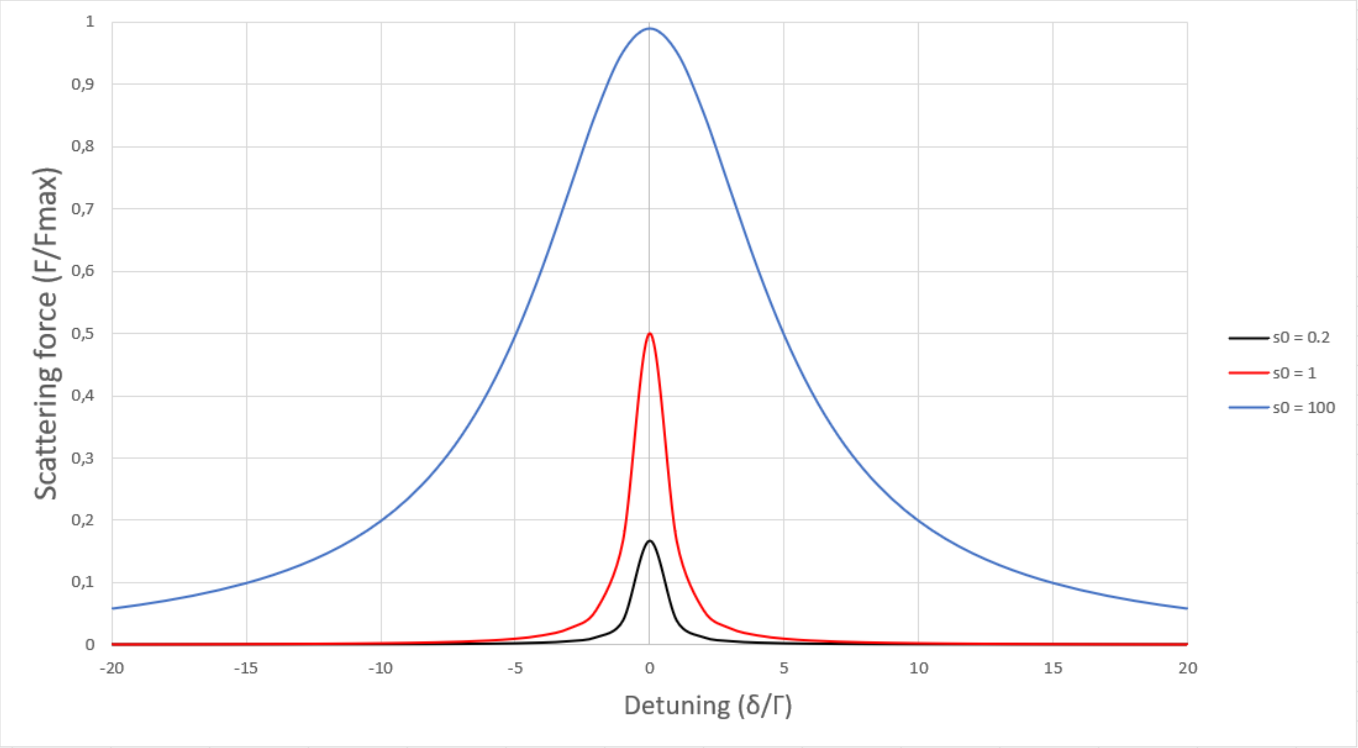

Figure 2-2. Laser cooling scattering force as a function of the detuning

An atom moving at a velocity v will see an additional detuning $k \cdot v$ due to the Doppler effect. The scattering force is then a function of the atom's velocity:

$$\boldsymbol{F} = \frac{\hbar k \Gamma}{2}\left(\frac{\frac{I}{I_{sat}}}{1+\frac{I}{I_{sat}}+\frac{4(\delta-k\cdot v)^2}{\Gamma^2}}\right) \tag{2.22}$$

We can again rewrite this function to show that, for a beam propagating along the same direction as the atomic motion, the force is maximized for $k \cdot v = \delta$.

$$\boldsymbol{F} = \frac{\hbar \boldsymbol{k} \boldsymbol{\Gamma}}{2}\left(\frac{\boldsymbol{I}}{\boldsymbol{I}+\boldsymbol{I}_{sat}}\right)\frac{\left(\frac{\Gamma}{2}\sqrt{1+{}^{\boldsymbol{I}}/_{\boldsymbol{I}_{sat}}}\right)^2}{\left(\frac{\delta}{k}-v\right)^2+\left(\frac{\Gamma}{2}\sqrt{1+{}^{\boldsymbol{I}}/_{\boldsymbol{I}_{sat}}}\right)^2} \tag{2.23}$$

When the laser field is red-detuned, $\delta < 0$, the scattering force can be used to slow and therefore, cool atoms. An atom with a Doppler shift $k \cdot v = \delta$ will scatter strongly from a counter-propagating beam, with the absorption of each photon of momentum $\sim k$ decreasing the atom's velocity along the beam axis by an average $v = \sim k/m$, the recoil velocity, until the velocity decrease brings the atom out of resonance. By absorbing the photon, this atom acquires a net momentum kick, but the momentum recoil from spontaneously emitted photons averages over all directions and gives no net momentum transfer.

This technique of cooling has a minimum limit. The Doppler limit for laser cooling gives the minimum achievable temperature for a given transition. Based on the transition rate, the temperature limit is:

$$T_{Doppler} = \frac{\hbar\Gamma}{2k_B} \tag{2.24}$$

Where Γ is the transition linewidth in Hz

2.1.4 Detection beam

We detect atoms that pass through a detection beam resonant with the $^1S_0 \rightarrow {}^1P_1$ transition by imaging fluorescence from spontaneous emission onto a photodiode. A laser excites atoms in the $^1S_0$ state to the $^1P_1$ state, and each relaxes back to $^1S_0$ after scattering a photon in a random direction due to spontaneous emission. This cycle repeats, and on average, each atom scatters a photon every $\tau_{scat} = \frac{1}{\Gamma} \simeq 5ns$, for $I > I_{sat}$. The number of photons collected per atom depends on the time it spends in the probe beam, which is inversely proportional to its velocity. The number of atoms/secs in the beam can be calculated from the fluorescence signal by using the scattering rate, the velocity distribution of the beam, and the imaging and detector efficiencies.

2.1.5 π and $\pi/_2$ pulses

In order to explain what is a π -pulse and a $\pi/_2$ -pulse we have to come back to the equations of a two-level system. In particular, we have to go onto the momentum transfer induced by the electromagnetic field to the Two-level atom. The atomic states can be labeled by $|g, \boldsymbol{p_g}\rangle$ or $|e, \boldsymbol{p_e}\rangle$, where g and e represent respectively the ground and excited state. In the momentum basis, the spatial dependence arises via the translation operator

$$e^{i\boldsymbol{k}\cdot\hat{\boldsymbol{x}}}|\boldsymbol{p}\rangle = |\boldsymbol{p} + \hbar\boldsymbol{k}\rangle \tag{2.25}$$

This equation expresses the well-known result whereby the absorption of a photon of wave vector k changes the atomic momentum by $\hbar\boldsymbol{k}$. The light field couples the quantum states $|g, \boldsymbol{p_g}\rangle$, and $|e, \boldsymbol{p_e} + \hbar\boldsymbol{k}\rangle$. A pulse of resonant radiation that has a duration of $t\pi = \pi/\Omega$ is called a π -pulse. Applying a π -pulse results in the complete transfer of population from one state to the other. For instance, an atom initially in $|g\rangle$ ends up in $|e\rangle$ after the pulse. We can express the two configurations of π -pulse and $\pi/_2$ -pulse by the following equations:

- Case 1: The $\pi/_2$ -pulse correspond to $\Omega t_{\pi/_2} = \pi/_2$:

$$|\Psi(t)\rangle = \frac{1}{\sqrt{2}}\left[|g, \boldsymbol{p_g}\rangle - i|e, \boldsymbol{p_e} + \hbar\boldsymbol{k}\rangle e^{-i\phi(t)}\right] \tag{2.26}$$

- Case II: The π-pulse with $\Omega t_\pi = \pi$:

$$|\Psi(t)\rangle = -i|e, \boldsymbol{p_e} + \hbar\boldsymbol{k}\rangle \tag{2.27}$$

Where the phase $\varphi(t) = \delta t$, with detuning $\delta = \omega - \omega_0$. When the atom is subjected to a $\pi/_2$ -pulse, the photon of momentum $\hbar\boldsymbol{k}$ puts it into a coherent and equal superposition of both energy states. The recoil imparted to the atom gives rise to two coherent wave packets (in each internal state) separated by a velocity $v = \hbar k/_m$. In other words, this $\pi/_2$ -pulse plays a role analogous to the 50-50 beam splitter in classical optics. In the same way, when the coupling parameters are chosen such that $\Omega\tau = \pi$ (a π-pulse), the probability of finding an atom in $|e, \boldsymbol{p_e} + \hbar\boldsymbol{k}\rangle$ after a time t is equal to 1; in this case the light pulse behaves like a mirror.

2.2 Atom interferometry theory

2.2.1 Gyroscope interferometer configuration

The configuration of our interferometer used for the gyroscope is represented in Figure 2-3.

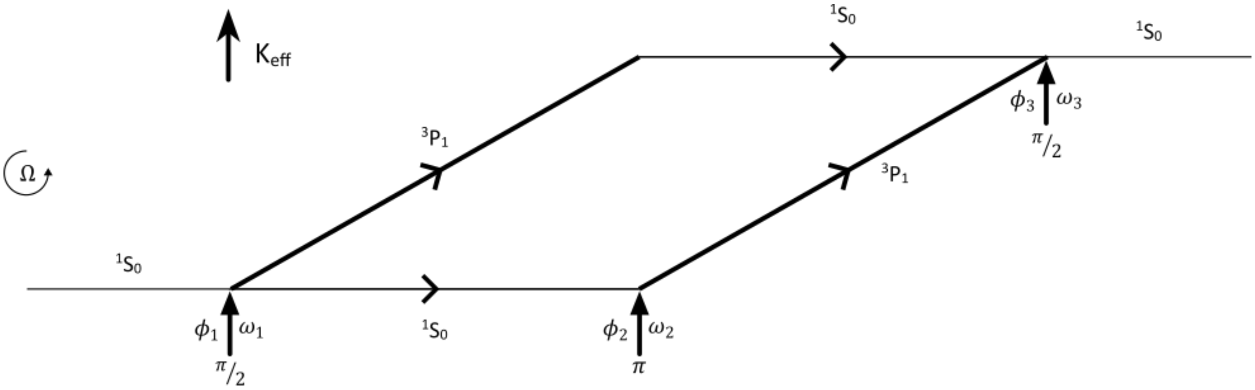

Figure 2-3. Configuration of our gyroscope's Atomic interferometer

Strontium atoms generated from the oven in a coherent thermal beam are initially in the ground state $^1S_0$. Then, they enter the interferometer and then pass through three laser beams. The first laser beam is a $\pi/_2$ -pulse. As explained before, this pulse affects the Sr atoms beam in two aspects. First, the $\pi/_2$ -pulse puts the atoms in a superposition of two states, in our case, $^1S_0$ and $^3P_1$. Second, the atoms excited in the $^3P_1$ state are subject to change in momentum. This modification arises from the principle of conservation of momentum during their interaction with the laser beam. Thus, the initial atom momentum will be combined with the laser beams transverse momentum, dividing atomic wavepackets in two trajectories. The second laser beam is a π-pulse. It acts as a mirror by swapping the atoms' momentums and states in the interferometer. This change in momentum redirects the two trajectories back toward each other. The last beam is also a $\pi/2$ beam that recombines the two trajectories, so interferences can occur. When the interferometer rotates, the atoms in the two paths acquire a phase shift. So, The interference is related to the measurement of the number of atoms in the $^1S_0$ state. Because each atom has its own relative phase, the interference phenomenon becomes a single-particle phenomenon.

To obtain and detect the interference particle initially in a state $|\psi_1\rangle$, it has to evolve into a superposition of two states.

$$|\psi_1\rangle \rightarrow |\psi_2\rangle + |\psi_3\rangle \tag{2.28}$$

So, the probability of detecting the particle in a final state $|\psi_F\rangle$ is given by the expectation value of the projection operator, $|\psi_F\rangle\langle\psi_F|$. Thus, We find:

$$P(\psi_F) = |\langle\psi_F|\psi_2\rangle|^2 + |\langle\psi_F|\psi_3\rangle|^2 + 2Re\{\langle\psi_F|\psi_2\rangle\langle\psi_F|\psi_3\rangle^*\} \tag{2.29}$$

The interference is represented by the cross term, which is sensitive to the phase shift carried by the atoms during their travel in the interferometer.

2.2.2 Phase shift calculation

In this section, we will discuss the phase shift calculation of our interferometer. The first part will cover the phase shift due to the matter-wave interaction, and in the second part, we will determine the phase shift due to the rotation.

2.2.2.1 Atom-light interaction induce phase shift

Let's consider our interferometer configuration sequence with atom-light interactions at times $t \in \{0, T, 2T\}$ and measure the induced phase shift between the two arms. We will now use the midpoint theorem to calculate each path's phases. The black arrows in Figure 2-3 represent the interferometer as a sequence of atom-light interactions. We will now fix the notation to make the calculation understandable. We define $x_{j,i}$ to be the displacement of arm j at the time of the ith pulse. We can also define the wavevector k_i, the frequency ω_i and the phase ϕ_i of the laser beam for the ith pulse interacting with the atoms and putting them into an effective coupling of two atomic states. The atom-light interactions in each arm j can either result in an absorption of a photon by the atoms (gaining internal energy $\hbar\omega_i$ and momentum $\hbar k_i$) or emit one photon, losing the same amount of internal energy or momentum). So, we can update our notation in $k_{j,i}$ for the wavevector $\omega_{j,i}$ for the frequency and $\phi_{j,i}$ for the phase of the ith interaction on the arm j. Thus, $k_{j,i} = \pm k_i$, $\omega_{j,i} = \pm\omega_i$, and $\phi_{j,i} = \pm\phi_i$, where the sign depends on the absorption (+) or emission (−) of a photon during the ith interaction on the arm j. Of course, if the interaction ith does not change in internal energy of the momentum of an atom on the arm j, $k_{j,i} = \omega_{j,i} = \phi_{j,i} = 0$. Atoms can exit the interferometer in one of two output ports, each of them which corresponds to a particular momentum state. The interferometer phase $\Delta\phi$ allows us to calculate the probabilities to find an atom in this particular momentum state according to the equation:

$$P = \frac{1}{2}(1 - cos\ (\Delta\phi)) \tag{2.30}$$

According to the midpoint theorem[26], the interferometer phase can be written as:

$$\Delta\phi = \sum_{i=1}^{3}[(k_{1,i} - k_{2,i})\bar{x}_i - (\omega_{1,i} - \omega_{2,i})t_i + (\phi_{1,i} - \phi_{2,i})] \tag{2.31}$$

Here the index i correspond to the N atom-light interactions, t_i is the time of the ith pulse, and the average displacement of the two arms with respect to the laser at time t_i is:

$$\bar{x}_i = \frac{x_{1,i}+x_{2,i}}{2} \tag{2.32}$$

In our case, we are in the Mach-Zehnder configuration for an interferometer is shown in Figure 2-4.

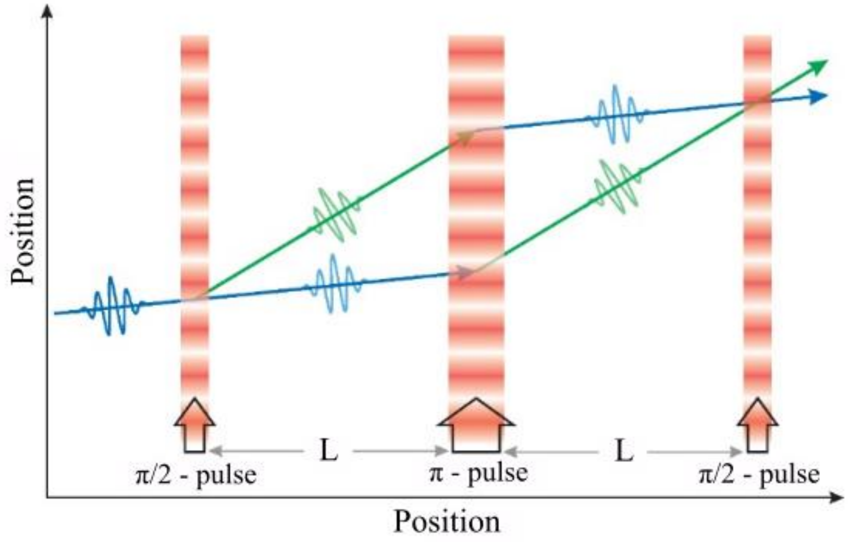

Figure 2-4. Mach-Zehnder Interferometer configuration

Thus, we are assuming that ϕ_i is constant for all I, and we are also using the fact that in a Mach-Zehnder accelerometer, the terms ω_i sum to zero because the two arms spend equal time in each internal state. So, we can express $\Delta\phi$ as

$$\Delta\phi = \sum_{i=1}^{3}(k_{1,i} - k_{2,i})\bar{x}_i \tag{2.33}$$

We can simplify the sum as follows:

$$\Delta\phi = k\bar{x}(0) - 2k\bar{x}(T) + k\bar{x}(2T) \tag{2.34}$$

Or we can also write it in term of phase:

$$\Delta\phi = \phi_1 - 2\phi_2 + \phi_3 \tag{2.35}$$

2.2.2.2 Rotation-induced phase shift

To calculate the phase shift due to the rotation, we have to use classical mechanics. Hamilton's principle states that the action of a particle traveling along the path Γ in an external potential V (r) is determined by the following integral

$$S_\Gamma = \int_{t_a}^{t_b} L[\boldsymbol{r}(t), \dot{\boldsymbol{r}}(t)]dt \tag{2.36}$$

where the Lagrangian $L(\boldsymbol{r}, \dot{\boldsymbol{r}})$is defined as $L(\boldsymbol{r}, \dot{\boldsymbol{r}}) = \frac{1}{2}m\dot{\boldsymbol{r}} - V(\boldsymbol{r})$.

In quantum mechanics, Feynman's path integral method [27] can be used to compute the probability of a particle at point a ending up at point b by summing the amplitudes of all paths from a to b. The phase acquired during the propagation of a particle along all these paths is ${}^{S_\Gamma}/_{\hbar}$. In our case, the particle is not submitted to an external potential, so the Lagrangian becomes $L(\boldsymbol{r}) = \frac{1}{2}m\dot{\boldsymbol{r}}^2$. Combining Feynman's path integral method and Hamilton's principle, we can express the rotation induced phase-shift as

$$\Delta\Phi = \frac{1}{\hbar}\oint_\Gamma \Delta L \, dt \tag{2.37}$$

Let's now determine the Lagrangian in our case. Consider an inertial coordinate frame and a frame rotating with angular frequency. The operator relating the rate of change of a vector r, describing the position of a particle in the rotating frame, in the inertial coordinate frame r' is:

$$\left(\frac{d}{dt}\right)_{inertial} = \left(\frac{d}{dt}\right)_{rotating} + \Omega \times \tag{2.38}$$

Applied to the vector r, it gives:

$$\left(\frac{d\boldsymbol{r}'}{dt}\right) = \left(\frac{d\boldsymbol{r}}{dt}\right) + \Omega \times \boldsymbol{r} \tag{2.39}$$

For a free particle in the inertial frame, the Lagrangian becomes

$$L' = \frac{1}{2}mv'^2 \tag{2.40}$$

Because the Lagrangian has the same value in both frames, we can rewrite it using the rotating frame coordinates as follows:

$$L' = L = \frac{1}{2}m(v + \Omega \times \boldsymbol{r})^2 = \frac{1}{2}mv^2 + m\Omega \cdot (\boldsymbol{r} \times v) + O(\Omega^2) \tag{2.41}$$

In the rotating frame, Coriolis acceleration adds a perturbation $\varDelta L = m\varOmega \cdot (\boldsymbol{r} \times v)$ to the free particle Lagrangian. We can now use the equation

$$\Delta\Phi = \frac{m\varOmega}{\hbar}\oint_{\Gamma}(\boldsymbol{r} \times v)\, dt = \frac{m\varOmega}{\hbar}\oint_{\Gamma}(\boldsymbol{r} \times d\boldsymbol{r}) \tag{2.42}$$

The integral is equal to 2A, where A is the area enclosed by the paths, since $r \times dr$ is the area of a parallelogram with adjacent edges defined by vectors r and dr. This results in the usual Sagnac phase shift expression:

$$\Delta\Phi_{\Omega} = \frac{2m}{\hbar}\Omega \cdot A \tag{2.43}$$

2.2.2.3 Total phase shift

We can express the total phase shift, in the laboratory frame, at the first order of the interferometer by applying the equations 2.35. In this case, the spatial propagation phase shift $\Delta\phi_{\Omega}$ cancels, and the rotation phase shift arises from the laser interactions. So we can write:

$$\Delta\phi_{tot} = \Delta\phi_{Atom-light} + \Delta\phi_{rot-interaction} \tag{2.44}$$

Using the Coriolis acceleration, this phase shift can be written as:

$$\Delta\phi_{rot-interaction} = -\boldsymbol{k}_{eff} \cdot \boldsymbol{a}T^2 \tag{2.45}$$

Where $T = {}^{L}/_{v}$ is the time spent between Raman beams and $\boldsymbol{a} = 2\Omega \times v$ is linear or Coriolis acceleration. We can rewrite this equation using the reference frame of the interferometer[28]:

$$\Delta\phi_{rot-interaction} = -\, 2k_x T^2 \Omega_z v_y \tag{2.46}$$

Where atomic beam propagate along the axis y and the lasers beams along the axis x. In the next notations we will keep the notation of equation (2.45). For a general inertial acceleration, we find a phase shift of [16], [27], [29]:

$$\Delta\phi_{tot} = -\boldsymbol{k}_{eff} \cdot \boldsymbol{a}T^2 + \phi_1 - 2\phi_2 + \phi_3 \tag{2.47}$$

Finally, the interferometer signal is the probability of finding the atoms in a specific state:

$$P = \frac{1}{2}\left[1 - \cos\left(-\boldsymbol{k}_{eff} \cdot \boldsymbol{a}T^2 + \phi_1 - 2\phi_2 + \phi_3\right)\right] \tag{2.48}$$

2.2.2.4 Rotation-induced Doppler shifts

In our interferometer, the center of rotation in the inertial frame is not the center of the interferometer, as shown in the following figure. Thus, the beams will be Doppler shifted by the rotation of the apparatus. This Doppler Shift can be written in the following form :

$$\delta = +k_{eff}\Omega L \tag{2.49}$$

Where L is the distance to the center of rotation, Ω the rotation rate and k_{eff} the wavevector of the beams. Figure 2-5 illustrates the doppler shift explained before.

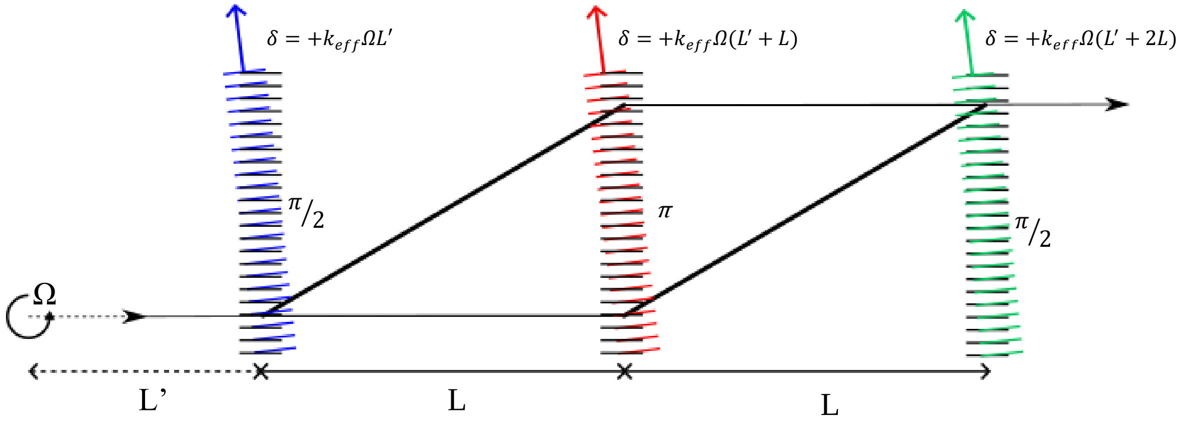

Figure 2-5. Interferometer configuration with Doppler shifted π and $\pi/2$ beams

In the case of our interferometer, $\delta_{1st\ beam} \simeq \delta_{Last\ beam}$ because $L' \gg L$. So, we can apply the same detuning for all the beams to compensate for this doppler shift. Note that the rotation-induced Doppler shift is independent of atom velocity and therefore is the same for both atomic beam directions. Position and angle changes of the π and $\pi/2$ beams are neglected since, for small rotation rates the position changes by a second order, and the angle change is smaller than the k-vector spread. Therefore, in the inertial frame, the π and $\pi/2$ beams may be treated as static but with Doppler-shifted $\pi/2$ and π beams detuning. The Doppler shifts can be compensated by detuning the beams by δ_f. The beams’ detuning implementation is described in Chapter 3[30].

CHAPTER 3 - Apparatus

3.1 Overview

A block diagram of the gyroscope setup is provided in Figure 3-1. Briefly, an oven produces a strontium atomic beam that propagates in an ultra-high-vacuum (UHV) chamber. The atomic beam is first cooled in one direction (1D cooling in Figure 3-1). At this point, a detector allows us to lock the blue laser at a suitable frequency. The atomic beam is then transversely cooled before entering the interferometer region. There, the atomic beam will see the π and $\pi/2$ -pulses laser beams serve to divide, deflect, and recombine the atomic wavepackets. The interferences created between the two paths through the interferometer allow the rotation-rate-dependent phase shift between the paths to be observed by detecting the number of atoms exiting the interferometer in a particular state, as measured by fluorescence from a resonant probe laser. In our case, the resonant prob laser will be the blue laser beam connected to the chamber in Figure 3.1. The apparatus measures the relative angular velocity between the inertial frame of the atoms in the atomic beam and the lab frame containing the optical table. To maintain the chamber in an ultra-high vacuum, a system of an ion pump and a valve is set up just after the chamber. The data processing is done on another table by a set of oscilloscopes. The blue and red laser beams are also generated on another table named “Red/blue optical system” in Figure 3-1 and launched to the gyroscope thanks to optical fibers. We will discuss it in the next section. Finally, our apparatus also uses rotations sensors to verify the value obtained by the interferometer and to eliminate the effect of the doppler shift on the π and $\pi/2$ -pulses laser beams. A photograph of the gyroscope alone is shown in Figure 3-2. The optical systems out of the gyroscopes and producing the laser beams will be shown in the following sections.

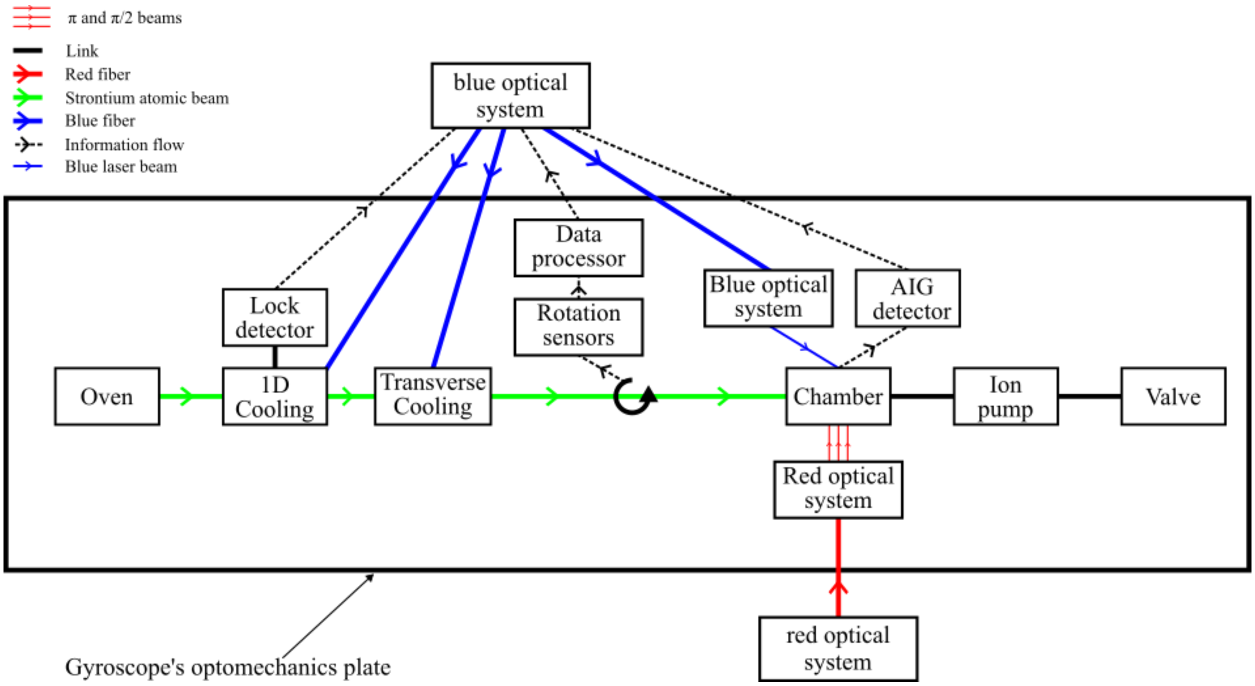

Figure 3-1. Block diagram of the Atomic Interferometer Gyroscope

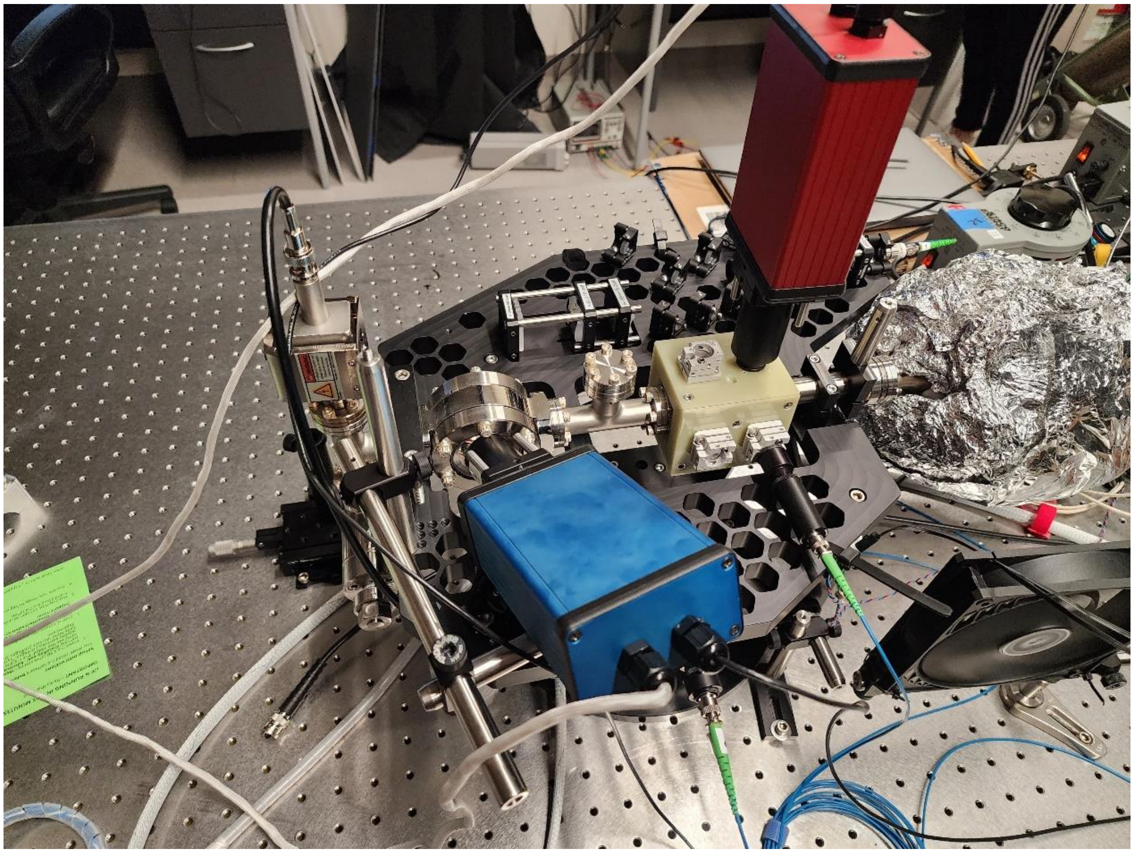

Figure 3-2. Picture of our Atomic Interferometer Gyroscope

3.2 Optical systems

3.2.1 Blue optical system

As discussed in the overview, the blue laser beams used for cooling and detection are generated in a specific optical system separated from the gyroscope. Figure 3-3 represent this system. Moreover, a photograph of this system can be shown in Figure 3-5.

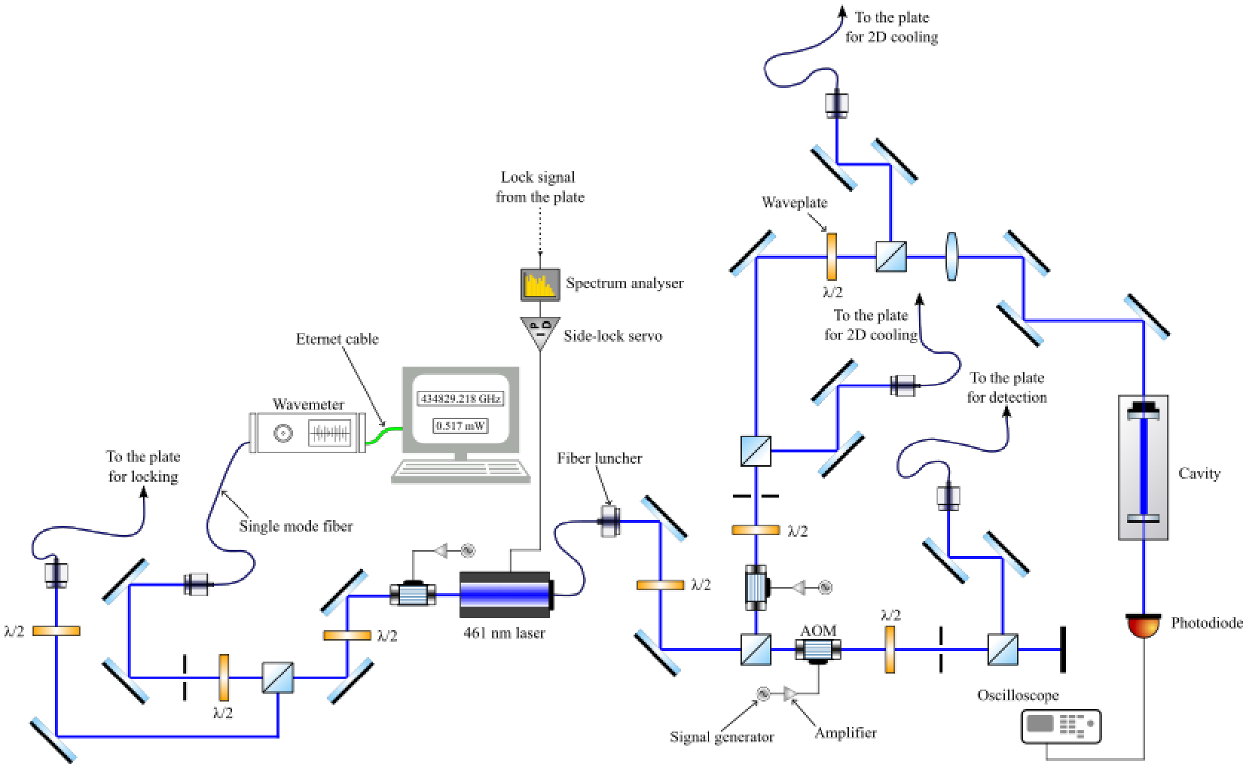

Figure 3-3. Schematic of the Blue optical system

In the case of the blue optical system, the laser beam is sent in two directions by a MOGLabs Injection Locked Amplified (ILA) laser. The wavelength used for the blue laser is 461 nm, as described in chapter 2. The laser beam sent in the left direction will directly reach an Acousto-Optic Modulator (AOM) connected to a signal generator and an amplifier that produces a frequency shift of 140 MHz. In the entire experiment, we use the model AOMO 3100-125 from the company “Gooch & Housego”. All our AOMs require an amplified signal because our signal generator AFG 1022 from the company Tektronix cannot reach the minimum input signal needed. The laser beam is then separated into two paths thanks to a beamsplitter. The waveplate controls the power going into the paths before the beamsplitter. The path in front of the incoming path goes to a wavemeter that doesn’t require much power to be efficient. The wavemeter allows us to control the beam’s frequency to match the required frequency. For the blue locking, the wavemeter is not the main tool to lock the frequency. Indeed, the other path provides the laser beam to the gyroscope for the 1D cooling and the blue locking system. This blue locking system is the main tool to lock at the good frequency. The laser beam sent to the gyroscope will force the atom to make the transition $^1S_0 \rightarrow {}^1P_1$, and by fluorescence, the detector will acquire a signal, as shown in Figure 3-4.

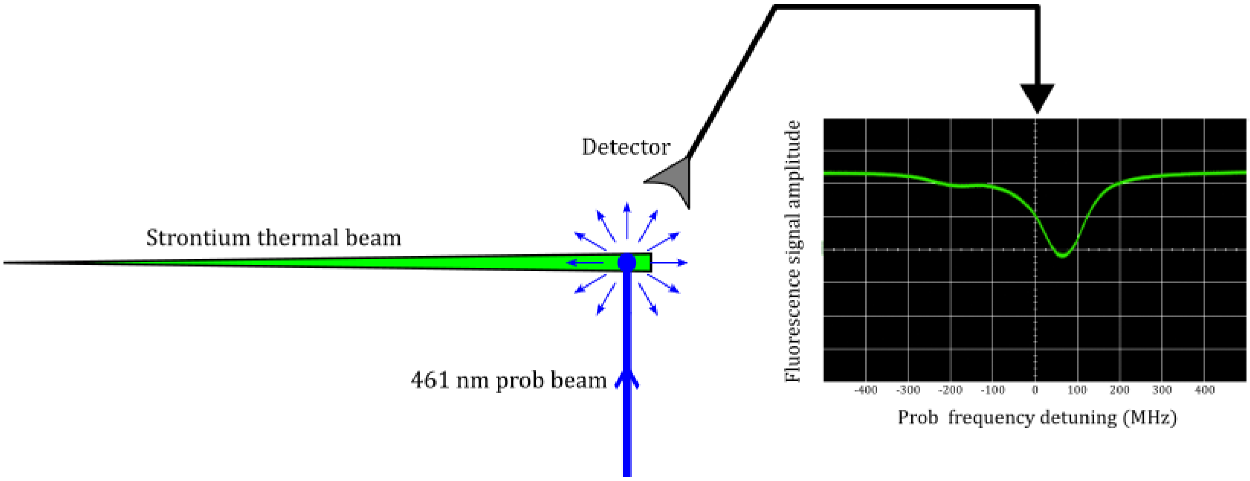

Figure 3-4. Scheme of the blue laser lock principle

This signal represents the fluorescence of the ^{88}Sr and ^{87}Sr as a function of detuning from the value expected. In our case, only the ^{88}Sr peak is relevant to us. Then, after analyzing the frequency shift, the detuning corresponding will be applied to the laser thanks to the side-lock servo, which is inside our diode laser controller from MOGLabs.

The beam sent in the right direction comes from the “back” of the laser, thanks to an optical fiber. This path is divided in two; in either case, the beam laser goes to an AOM. Because we do not have a full continuum of lasing modes in the laser diode, we have a shift on the seed for tunability, allowing us to put a "good" lasing mode into resonance. And since, we shift the seed light in the laser, we have to shift the light. This path redirects the beam to a fiber launcher sending the laser beam to the gyroscope. This laser beam will be used for detection and require high power.

The beam going in the upper AOM on the diagram sees a frequency shift of 125MHz. This frequency has been determined by maximizing the detection signal on an oscilloscope. This laser beam is separated and sent to the gyroscope for transverse cooling. At the end of this path, there is an Fabry-Perot (FP) cavity and a photodiode linked to the oscilloscope. Because this laser is injection locked, the cavity and the diode are just used for monitoring.

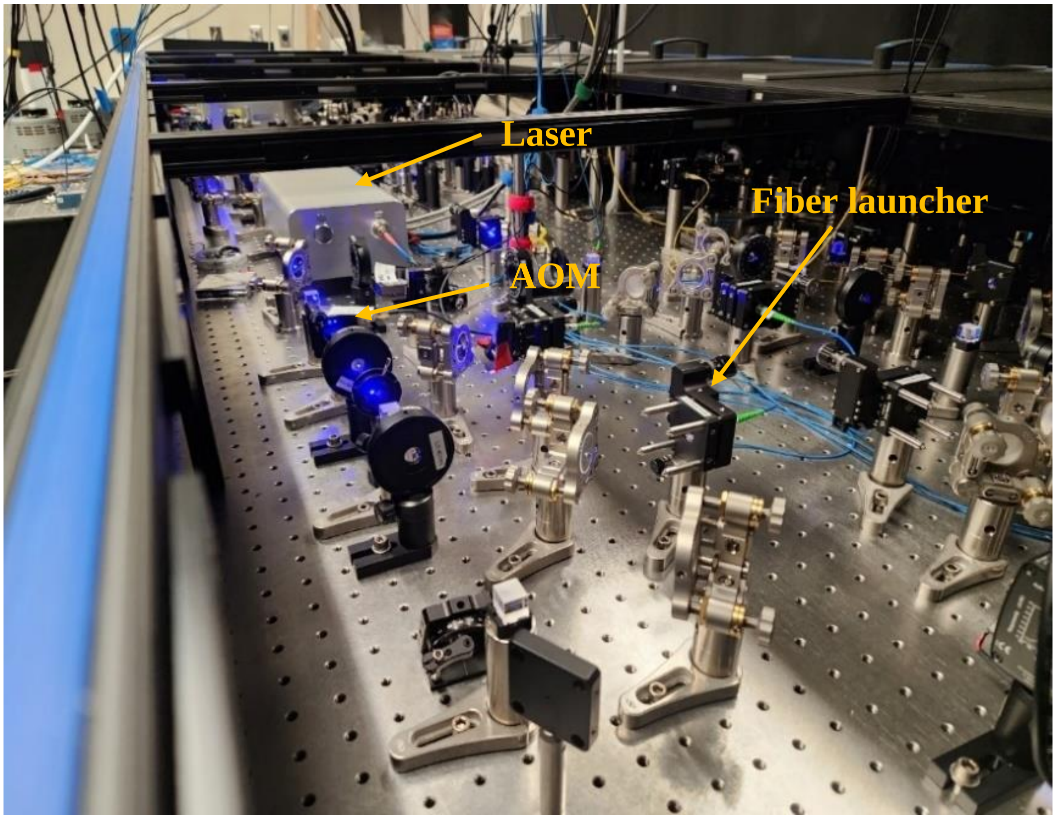

Figure 3-5. Picture of the Blue optical system

3.2.2 Red optical system

The red optical system produces the π and $\pi/2$ -pulses laser beams in order to divide, deflect and recombine the atomic beam. As for the blue optical system, a scheme of this system is represented in Figure 3-6. A picture of this system is also shown in Figure 3-9.

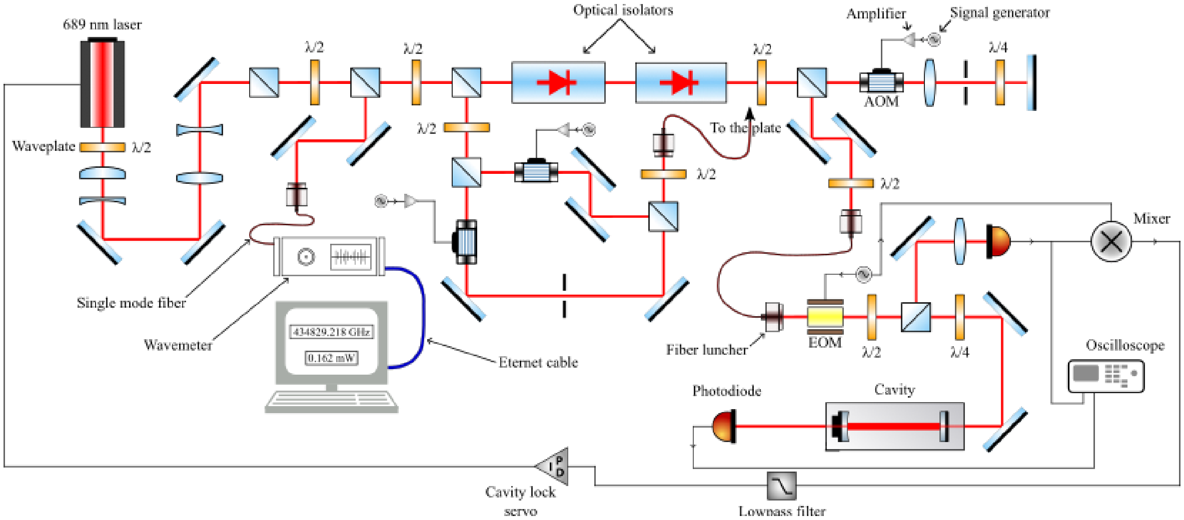

Figure 3-6. Schematic of the red optical system

The 689nm laser is a MOG CEL purchased from MOGLabs that can operate in the range of wavelength needed. The beam created by this laser has a size of 0.6 x 0.3mm. However, the beam size expands as it travels in the system. So, a system of two cylindrical lenses first reduces the beam size in the vertical direction. Thus, the size on the vertical axis will be reduced from 0.6 mm to 0.3 mm. The beam becomes circular but still expanding. After the second mirror, the system of two cylindrical lenses collimates the beam for the rest of the system.

This red optical system can be separated into three sub-systems but still use the same initial red laser beam. The first sub-system comes after the second beamsplitter. The laser beam is redirected to the wavemeter by a set of fiber and fiber launchers. Unlike the blue optical system, the wavemeter of this system is essential for the lock of the frequency. Indeed, the frequency needed remains the same at this point in the system and is not modified by an external factor. The frequency value used for the locking of the red laser is 434829.218 GHz, which corresponds to a wavelength of 689.449nm, as expected. Like in the blue optical system, the wavemeter doesn't require much power, and the waveplate regulates this power before the beamsplitter.

The second sub-system is the set-up of the π and $^{\pi}/_{2}$ -pulses laser beams. After the third beamsplitter, the laser beam is separated into two other beams by another beamsplitter with a perfect perpendicular polarization. Each beam, π or $^{\pi}/_{2}$, will enter an AOM (same used in the blue optical system). For the $^{\pi}/_{2}$ beam, the AOM will compensate the doppler shift induced by the rotation. This compensation process will be discussed in a next section. In the case of the π beam, the frequency shift applied on this beam using the AOM is composed of two parts. Of course, the π beam will be frequency-shifted to compensate for the doppler shift as with the $^{\pi}/_{2}$ beam. Moreover, the π beam has been chosen to carry another phase shift. This phase shift will help us analyze the phase shift induced by the rotation more precisely.

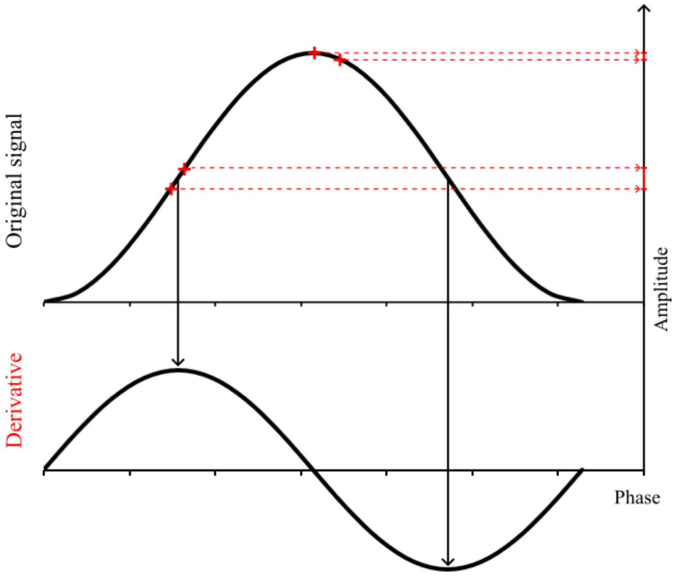

Figure 3-7. Diagram representing the side-of-fringe signal maximization principle

As shown in Figure 3-7, shifting the frequency will shift the phase, and a phase difference will have a bigger derivative amplitude on the side of the curve than on the top of the curve. Then, our result will be more precise.

After these AOM, both beams will be recombined thanks to a beam cube and sent to the gyroscope through a fiber. A polarization cleaning for these two beams is essential because it avoids the mixing of the beams in the fiber. This can cause the AIG signal to be contaminated by an interference signal due to polarization mixing.

The last section is separated from the others by two optical isolators. They prevent the precedent sections from being contaminated by the last one because the cavity and the double path can reflect and send back a small amount of light in the first two sections. So, this can shift the frequency of the π and $\pi/2$ beams. This section is made of a double path with an AOM set up with a 77 MHz frequency shift used to match the resonance frequency of our cavity from the "Stable Laser System" company. Then, the resulting laser beam will be sent to the cavity for locking. This locking system uses the Pound–Drever–Hall technique[31]. Light from the fiber launcher is sent through an EOM and is then directed upon the cavity. The beamsplitter and λ/4 plate act in combination to discriminate between the two directions of light travel: light traveling in the direction to the cavity, while light traveling in the direction from the cavity to the beamsplitter is diverted toward the photodetector. The EOM is driven by a signal produced by the signal generator. This impresses sidebands onto the laser light. Light reflected off the cavity is measured using a photodetector. The reflected signal consists of two unaltered sidebands and a phase-shifted main band. The photodetector signal is demodulated (passed through the mixer and the low-pass filter) to produce an error signal. This resulting electronic error signal measures how far the laser main band is off resonance with the cavity. It is used as feedback for active stabilization. The

Cavity lock servo error converts the error signal into a voltage that is fed back to the laser to keep it locked on resonance with the cavity.

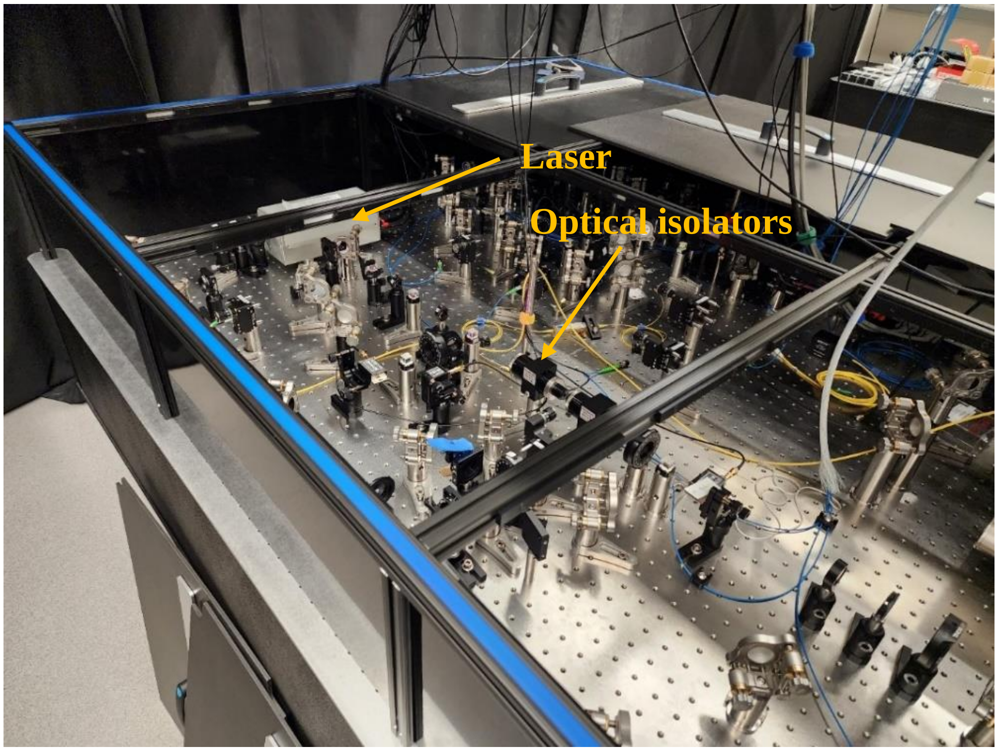

Figure 3-8. Picture of the red optical system

3.3 Gyroscope

3.3.1 Design

The design of our gyro is composed of two parts: the mount and the plate. On the plate will sit the chamber, and a blue and a red optical system are located on the sides of the chamber. In the following figure, you can see the mount on which the plate will sit.

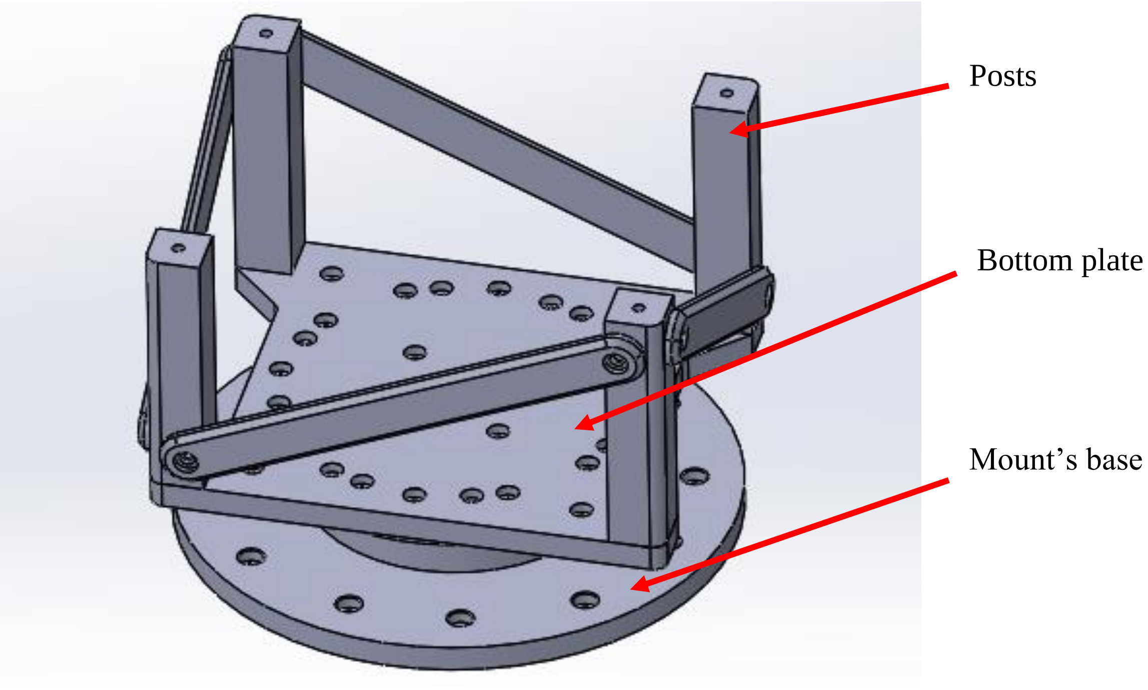

Figure 3-9. Design of the gyroscope mount

This mount is made of a base fixed to a vibration/tilt-insensitive table by screws to prevent vibration. The system Posts/Bottom plate can rotate thanks to a ball-bearing, model FMB-100-180 from the company PM bearings, between the base and the bottom plate. The design of the ball bearing is shown in Figure 3-11. The inner part of the bearing is fixed to the base, and the outer part is fixed to the bottom plate by screws. The outer part of the bearing is slightly elevated to avoid friction between the fixed base and the rotating part of the gyroscope.

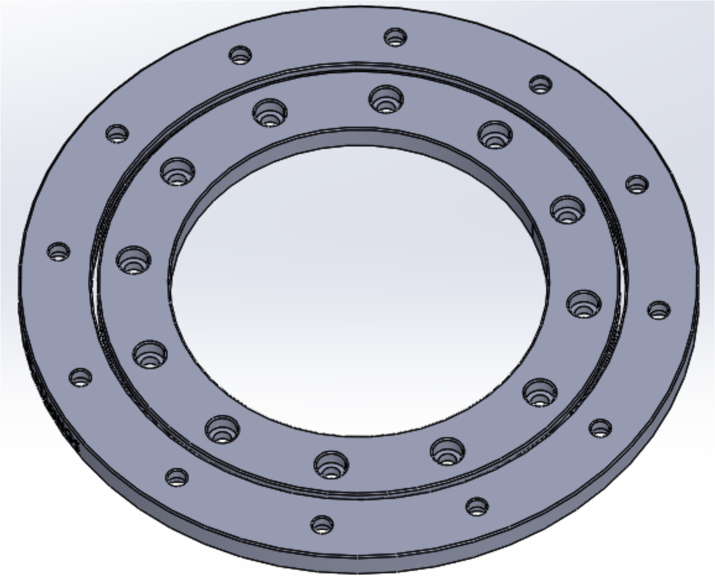

Figure 3-10. Design of the ball-bearing used for the mount. Model FMB-100-180 from https://www.pm.nl/

The posts carry the AIG plate and are maintained by transversal fixations used to maintain the AIG plate's stability and avoid any tilt. A top view of the entire AIG plate design is shown in the following figure and will be discussed in the next sections, part by part. Note that the AIG detector and its posts are represented as transparent to see the blue optical system.

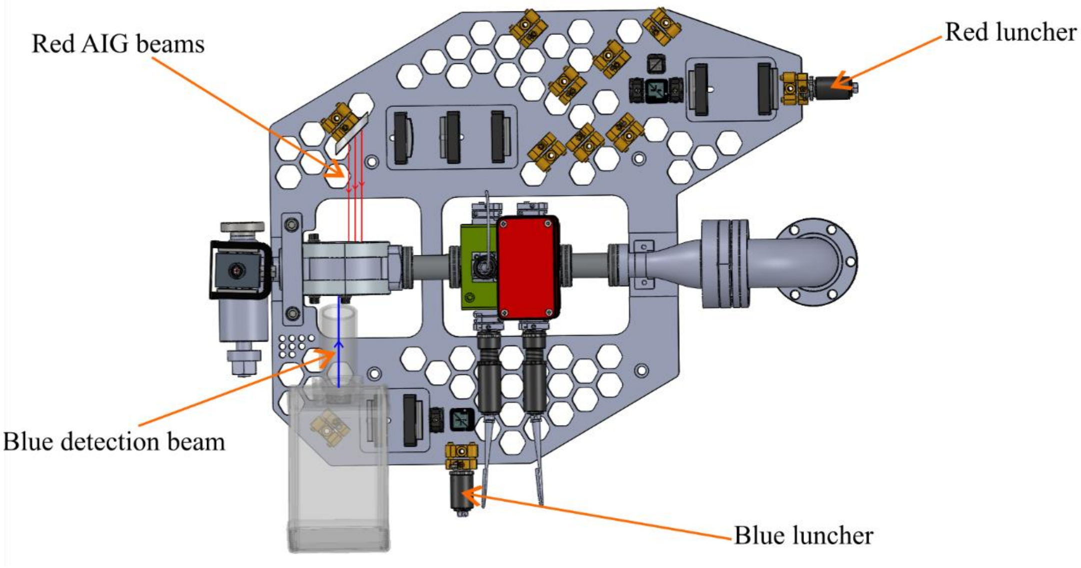

Figure 3-11. Rotating top plate with the chamber and the two optical systems

3.3.2 Chamber system

We will now discuss the chamber system. The following figure shows the design of the chamber set. The next sections will cover each part of the chamber system.

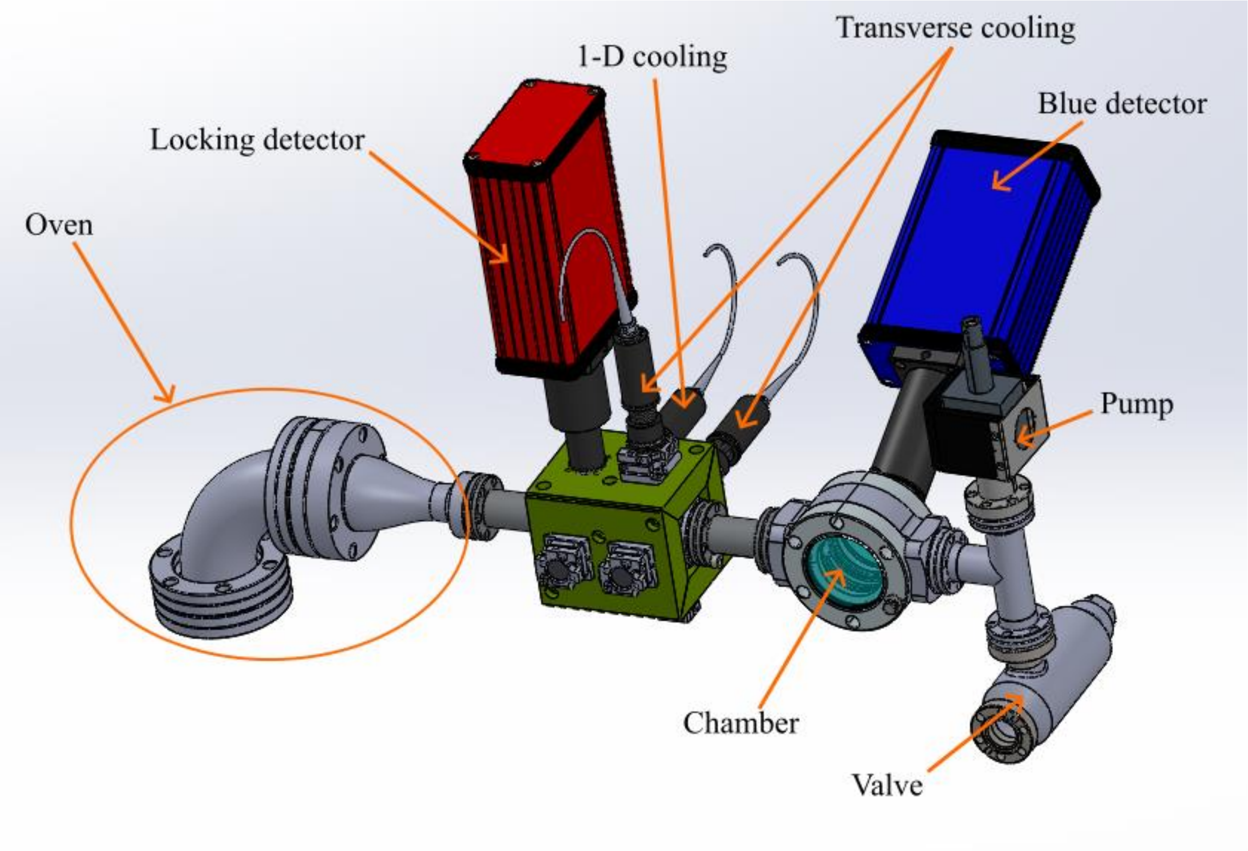

Figure 3-12. Design of the chamber system

3.3.2.1 Oven

A schematic of our oven is represented in Figure 3-14. A cylinder is fixed to a flange in the bottom of the elbow to hold strontium granules of natural abundance in 90% purity. Band heaters warm the elbow flanges, and so the crucible to the temperature of 430°C. This heating of the strontium granules raises the vapor pressure. This causes the strontium to effuse into the elbow and toward a nozzle.

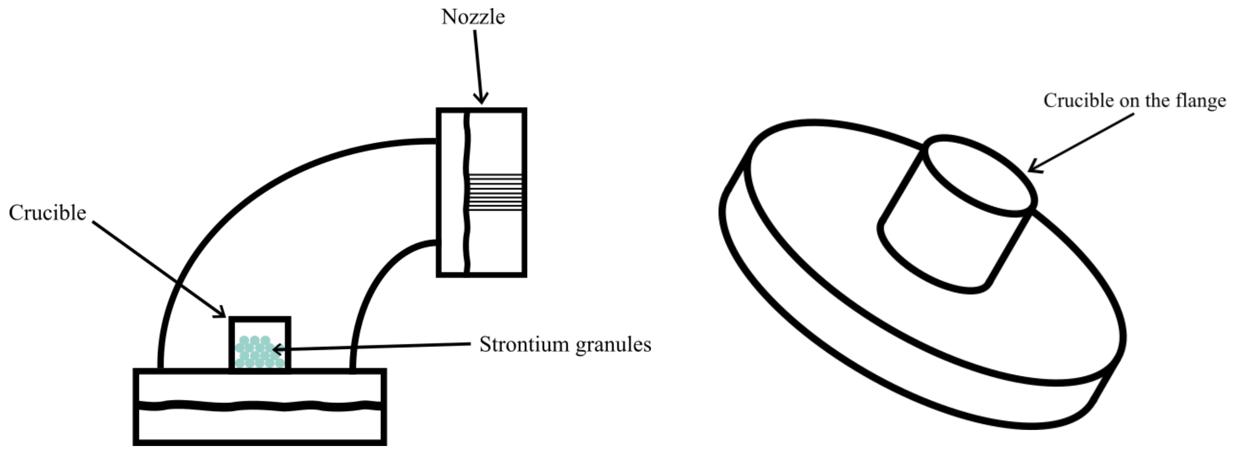

Figure 3-13. Scheme of the oven used for our gyroscope

The nozzle is a double-sided flange with a triangle hole cut out of the center, shown in Figure 3-16[32]. The aperture is a regular triangle with 4mm sides. The top of the aperture is a clamp that holds an array of microcapillary tubes to provide a collimated thermal beam from the effusing Sr gas. The following figure shows a simulation of particle trajectories through a microtube. In this simple simulation, the particles enter at random angles. This simulation also assumes that each collision redirects the particles with a random angle. The paths colored in blue are particles coming back into the oven, and the red paths are particles directed toward the chamber. Those particles that do not pass all the way through the tube without striking the walls have a higher probability of exiting the tube on the left because they are likely to strike the walls before reaching the middle of the tube. Thus, the exit beam is quite collimated, and most particles that would not enter the cooling region are recirculated to the oven reservoir.

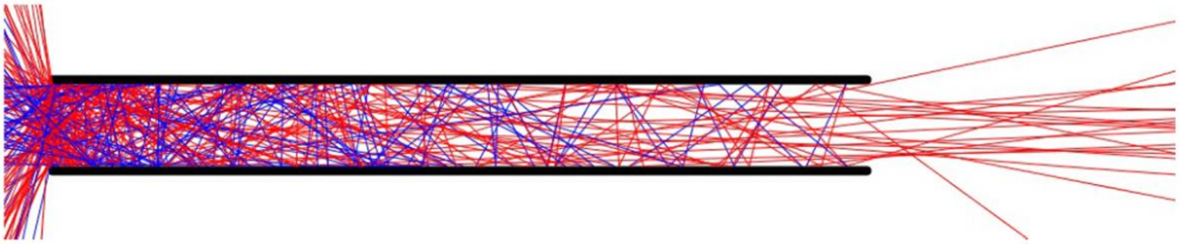

Figure 3-14. Simulation of the atoms behavior after entering in a microtube. Figure reproduced from [32].

To prevent clogging of the capillaries, the nozzle has to be the hottest point of the oven. Thus, it is kept at a temperature of 40-50C higher than the crucible. The elbow portion is also heated using heaters tape wrapped around the body.

The entire oven is then wrapped in fiberglass and aluminum foil to provide insulation and protection. The oven is connected to a step-down nipple used to go from a nominal diameter (DN) 35 to DN16, where a 4mm aperture is placed to help further maintain beam collimation. Indeed, the particles having a high angle compared to the axis of propagation wanted will be stopped by the aperture (i.e., optical aperture). It also reduces the effect of the oven outgassing on the overall pressure in the chamber and minimizes the stacking. The fan also helps a lot with this and allows the heat to not propagate in the chamber where the laser beams could be impacted. The flux produced by our oven is $\Phi \approx 1.32 \times 10^{10} atoms/s$. The derivation of this result is the same as in the chapter 4 using a signal of 1.6 V.

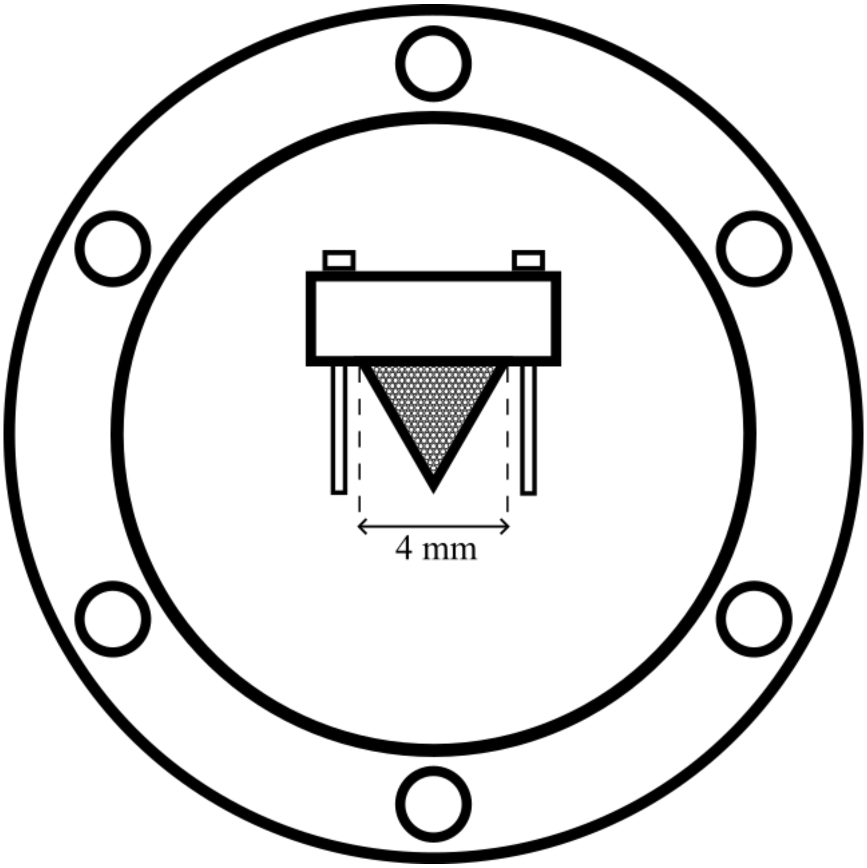

Figure 3-15. Scheme of the oven nozzle

3.3.2.2 Transverse cooling

The next section after the oven is dedicated to the blue locking and cooling. There are two types of cooling systems at this location. Two of the first three windows are used for the 1D transverse cooling beam. The goal of transverse cooling is to increase the number of atoms participating in the experiment by reducing the width of the atomic beam. The principle of this 1D transverse cooling is represented in Figure 3-17. The 1D cooling system acts on the x-axis, where the direction of propagation of the atoms is along the y-axis, and the z-axis is perpendicular to the plate's plane. The light is launched for a fiber launcher composed of a lens and a length adjustable tube to make the lens/fiber distance equal to the focal length of the lens. Thus, the beam is collimated with the size needed to maximize the cooling. As discussed in section 1.2.2, the blue laser beam is detuned by 140 MHz out from resonance. The beam size for this cooling is 3.2 mm radius. Moreover, this cooling is retroreflected with a mirror fixed on the window in front of the fiber launcher so the beam can be cooled in the two directions on this axis.

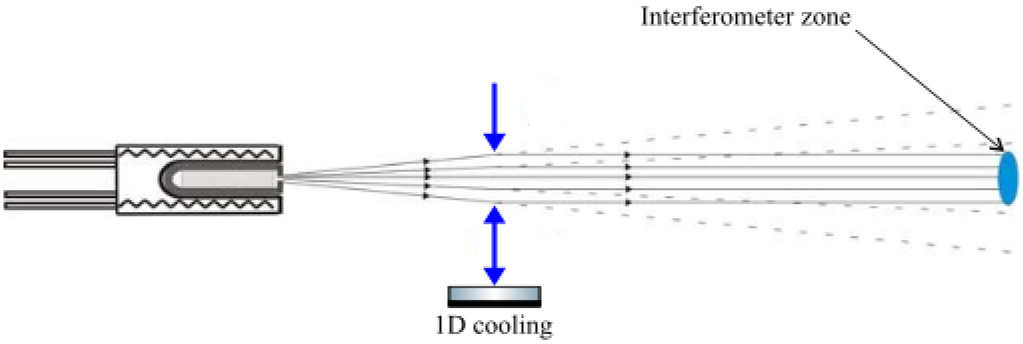

Figure 3-16. Scheme of 1D transverse cooling

The following four windows are dedicated to the two retroreflected beams for 2D transverse cooling. This cooling system has the same design as the 1D transverse cooling system but on the x and the y-axis. The collimators used are the same used for the 1D cooling too. This time the detuning frequency is 125 MHz. The values for the frequency detuning were determined by maximizing the detection signal. At the end of this section, a second 4mm aperture further maintains atomic beam collimation.

3.3.2.3 Chamber and vacuum system

The experiment must be carried out in an ultra-high vacuum (UHV) environment so that strontium atoms are not perturbed by collisions with background gas during their transit time across the apparatus. The chamber is made of vacuum-resistant windows and pieces. At the end of the apparatus and directly connected to the chamber, the vacuum system is made by a vacuum pump and a valve.

The ion pump used is the TiTan ion pump. Our ion pump works at high voltage, and when the oven temperature is stable, the chamber is under a vacuum of $2.4 \times 10^{-7} Torr = 2{,}67 \times 10^{-11}\ bar$. The vacuum valve is placed just bellow the ion pump. This vacuum valve is used when the chamber is put under High Vacuum by a turbo pump. Once the chamber is under high vacuum, the turbo pump the valve is closed and the turbo pump is removed from the apparatus. So, the ion pump can finish to put the chamber under Ultra High Vacuum.

3.3.2.4 Detection

Lock detection and AIG detection use the same principle: the fluorescence of the atoms after releasing a photon due to their excitation by laser light is sensed by a detector and interpreted as a signal on the oscilloscope. The detector is placed perpendicularly to the plate's plane for lock detection. It is maintained thanks to the box of the cooling system. The laser beam used to excite the atoms is the same as used by the 1D transverse cooling. The AIG detector is, on its side, placed after the chamber window facing with a little angle the π and ${\pi}/{2}$ laser beams. This angle is chosen to maximize the fluorescence signal on the oscilloscope. The AIG detector is maintained at this angle by three half-inch posts from Thorlabs screwed to the plate. The detector used in both cases is the Hamamatsu APD module series C12703. This detector has a photosensitive area of 3 mm radius and a photosensitivity of $2 \times 10^{7}\ V/W$

3.3.3 Opto-mechanical plate

The plate is the element on which the chamber and the optical system sit. The schematic of the plate is represented in figure 3-19. The design of the plate minimizes its mass while considering the space required to put all the elements needed on it. The hexagonal holes are used to reduce the mass of the plate to reduce the Coriolis mass. Because the beams coming from the optical systems have to be launched perfectly in the center of the chamber and the radius being larger than the height of the beams compared to the plate, these holes in the middle of the plate allow us to position the center of the chamber at the good height. The blue and red beams are counter-propagating and are manipulated to fit the good size for the interferometer.

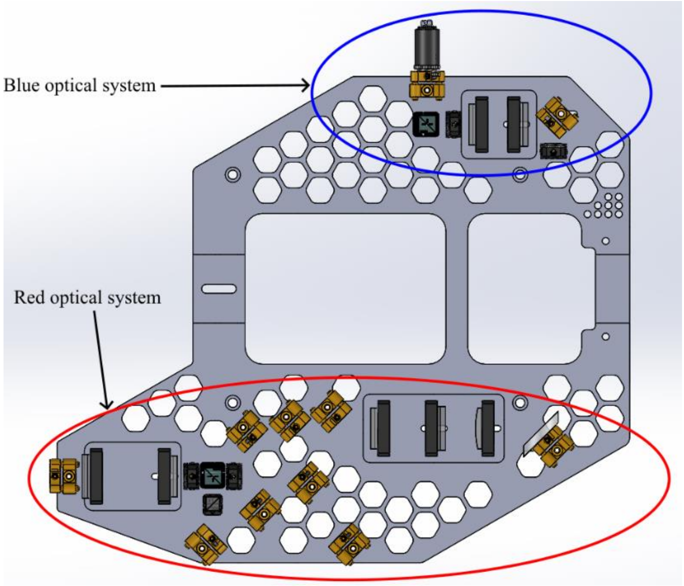

Figure 3-17. Rotating plate with the optical systems alone

3.3.3.1 Blue optical system

The Blue optical system, as shown above, is the smallest one. This system manipulates the beam size of the detection blue laser beam. The AIG detector is also on this side of the plate, so the optical elements must not to be in contact with it. This is why some room has been made between the center of the plate, where the chamber is, and the last optical element.

The laser beam comes from a single-mode fiber. It is collimated to a beam size of 1mm radius by the fiber launcher. Next, the beam is redirected by a beamsplitter, also used with the waveplate after that for polarization cleaning. The beam is expanded on the y-axis to make it match the size of the atomic beam. This expander is a three-times beam expander made of two lenses from Thorlabs: the first one is a plano-concave cylindrical lens with $f = -20.01\ mm$ and the second one is a plano-convex cylindrical lens with $f = 59.99\,mm$. Then a movable mirror and a waveplate are placed to redirect the beam perpendicular to the window of the chamber.

3.3.3.2 Red optical system

The π and $\pi/2$ laser beams are created on the red optical system. As for the blue, the red beam comes from a fiber and is launched by a collimator F-HS-NIR-APC purchased from Newport into the red system. After measurement, the collimated beam has a size of 0.9 mm radius and a beam divergence $< 0.5\,mrad$. So, the expansion is negligible over the distance traveled by the beam in this system. The beam size required for the red lasers beams is determined by the Rabi frequency. As seen in the theoretical background,

$$\frac{2\Omega^2}{\Gamma^2} = \frac{I}{I_{sat}} \tag{3.1}$$

So, we can rewrite this equation as:

$$\Omega(t) = \sqrt{\frac{I(t)}{I_{sat}}\frac{\Gamma^2}{2}} \tag{3.2}$$

The intensity can be rewritten as a function of time because we know the velocity of the atoms: 380 m/s. And,

$$\int_t \Omega(t)\,dt = \pi \text{ or } \frac{\pi}{2} \tag{3.3}$$

After integration, in the case of an ellipse, the size of the beam on the horizontal axis has to be 50 micrometers radius. The value chosen on the vertical axis for this calculation is 1.8 mm radius. In our case, the width of the beams will not be the discriminant factor between the π and $\pi/2$ beam types. Indeed, the beams will be the same size, but it is the intensity that will differentiate them. The power balance between these two beams is the following: $2P_{\pi/2} = \sqrt{2}P_\pi$

In a concern of space that we will discuss later, the beam size is reduced to 0.6 mm radius by a beam reduced on all the axes made of two spherical lenses with $f = 150\,mm$ and $f = -100\,mm$. The waveplate after this beam reducer corrected the polarization of the beam. This waveplate is essential because it allows us to reduce the mixing of the light and so perfectly separate the π and $\pi/2$ beams. Recall that these two beams have been combined by a beamsplitter in the Red optical system before the gyroscope. Thus, the next polarized beamsplitter separates the two types of beams. The beam going in front in Figure 3-19 is the π-beam that will be placed by two mirrors in the middle. The beam going down in Figure 3-19 is the $\pi/2$-beam, separated in two by a non-polarized beamsplitter. These beams are positioned by the mirrors on the left and right of the π beam. The separation between this beam is set to 7mm. This value comes from the decay time of the $^1S_0 \rightarrow {}^3P_1$ Sr transition. Indeed, the decay time constant can also be interpreted as the half-life of this transition. So, at least more than half of the atoms will remain in this state before the next pulse. In the case of this transition, the decay time is 21 µsecs, and the velocity of the atoms is around 380 m/s.

The following two lenses will set the beam size to 1.8 mm on the vertical axis by using a three-times beam expander with two cylindrical lenses of $f = -20.01\,mm$ and $f = 59.99\,mm$. The last lens of this system will make the beam convergent on the x-axis. By using the relationship between the beam waist at the focal point and our initial beam size, we can calculate the distance between the center of the chamber and the lens:

$$f = \frac{\pi w_0 w\prime}{\lambda} \tag{3.4}$$

Where f is the focal length needed, w0 is the beam waist before the lens, and w’ is the beam waist wanted at the focal point. In our case, $f = 136\,mm$. The reason why we reduce the beam with the beam reducer comes from this equation. With a bigger initial beam waist, the focal length is bigger, and we have to increase the size of the plate. Because this precise wavelength is not provided by the lens companies, we use a lens with a close wavelength: $f = 130\ mm$. The beams being too close to each other, the suitable lens width is not provided by the lens companies too. So, we cut this lens into three parts and fixed them to the same mount. During the cutting, the lens was protected against damage. A picture of the resulting beams is shown in the following figure. The last mirror is an elliptical mirror that redirects the beams to the chamber.

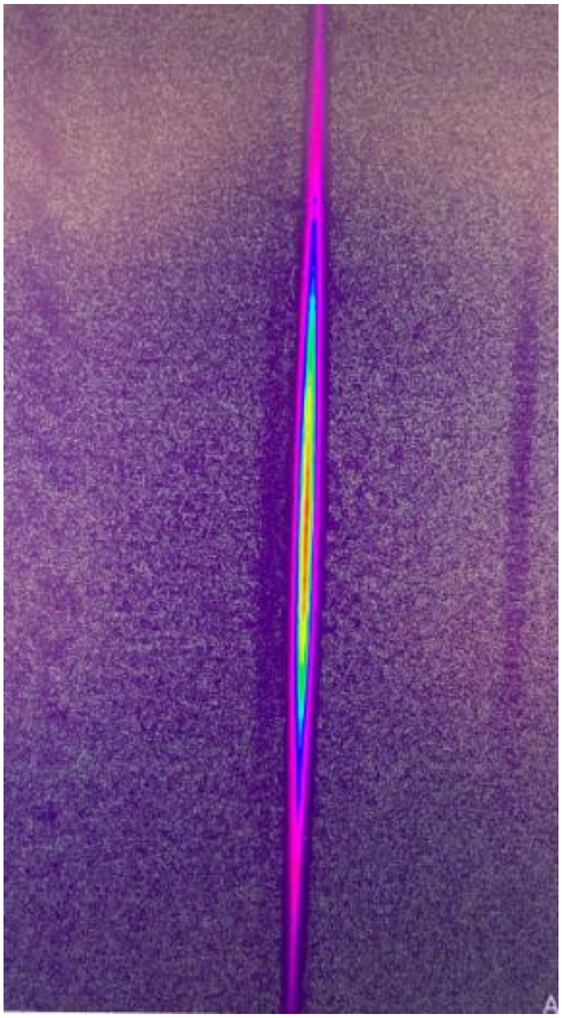

Figure 3-18. Picture of the π beam after manipulation on the plate

3.3.4 Feedforward and signal extraction

Feedforward is an essential feature of our apparatus. The plate rotation Doppler shifts the π and $^{\pi}/_{2}$ laser beams relative to the inertial frame of the atoms. This will no longer allow us to work on the side of the fringe because a new phase shift will appear due to the rotation that is not a part of the rotation-induced phase shift. So, if we compensate for these Doppler shifts by adjusting the beam detuning of π and $^{\pi}/_{2}$ laser beams, we can cancel this new phase shift and work on the side of the curve where the signal is larger. In this case, the atoms once again see zero detuning for each beam. A block schematic of the proposed signal extraction system and feedforward system is illustrated in Figure 3-21.

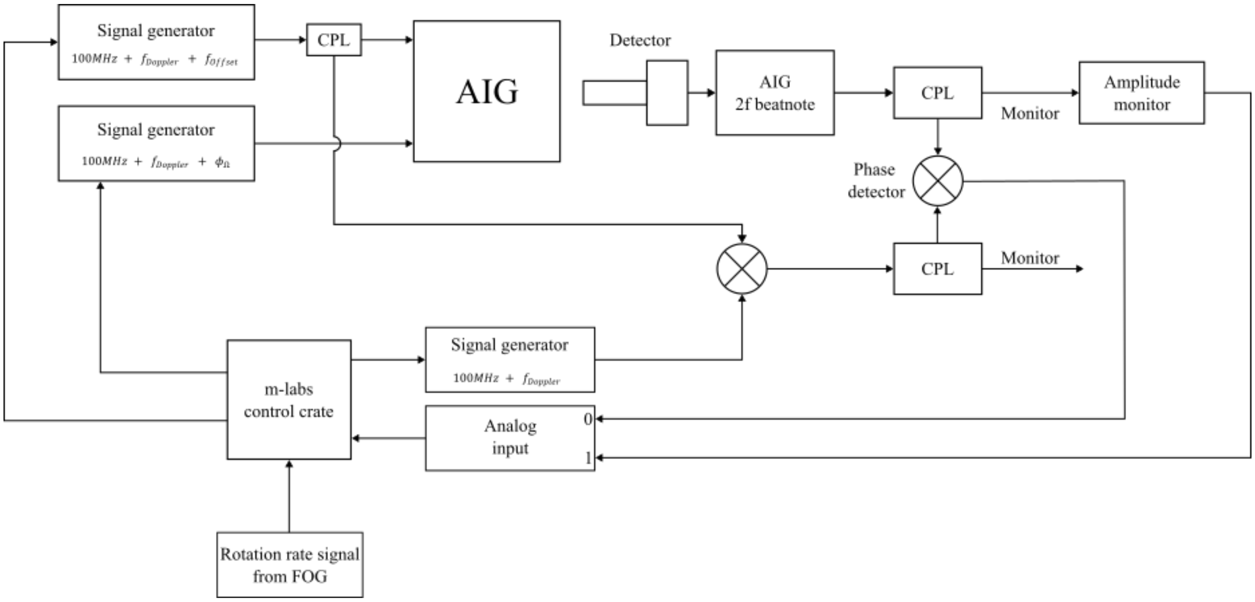

Figure 3-19. Box diagram of the signal extraction and feedforward systems

When the gyroscope starts spinning, a Fiber Optic Gyroscope (FOG) or an encoder gives a rotation rate signal sent to an M-lab controller. This controller calculates the frequency shift due to the rotation named $f_{Doppler}$ in Figure 3-21. Then, the signal generator sends the good frequency to the AOMs of π and $\frac{\pi}{2}$ beams. Then, the detector acquires the AIG signal analyzed with the beat note method. This method will compare the resulting interferences between the AIG signal with the rotation rate phase shift and the signal without this phase shift.

On the other side, the driving frequency sent in the $\frac{\pi}{2}$ beam AOM will be recovered. The 100MHz and the $f_{Doppler}$ will be recovered from another signal generator and the f_{offset} from the $\frac{\pi}{2}$ dedicated AOM signal generator (DDS 0). These two signals will be monitored, mixed, and compared to the AIG signal. Monitoring the AIG signal alone is important because, with the comparison, the amplitude information will be lost.

3.3.5 Encoder

The role of the encoder is to record a rotation rate reference and compare it to the AIG rotation rate. The encoder chosen for this experiment is the model. The encoder is situated at the bottom of the gyroscope. It is fixed to the base of the gyroscope that doesn't rotate. The rotating shaft, on its side, is fixed to the rotating bottom plate. So, the shaft, rotating element of the encoder, can freely rotate with the plate while the rest remain fixed. A picture of the encoder is shown in the following figure.

Figure 3-20. Picture of our encoder. Picture from encoder.com, Model 775A.

This encoder produces a squared signal where the frequency varies as a function of the rotation speed, so:

$$f = CPR * RPS \tag{3.9}$$

Where the Count Per Revolution (CPR) is the number of times the sensor disk is divided by, and RPS is the number of Rotation Per Second. Every division on the sensor disk will change the value of the signal from 0 to 1 or 1 to 0. Our encoder has a CPR of 30000 and a maximum frequency of 100kHz. So the maximum speed the encoder can record is 3.33 RPS which is fast enough.

CHAPTER 4 - Proof of concept

Our gyroscope is a new concept in the way that using the atomic transition $^1S_0 \rightarrow {}^3P_1$ of the strontium atom for an Atomic Interferometer gyroscope has never been made. To be sure that this interferometer could work without rotation, we had to prove this concept. Thus, a fixed interferometer was made before designing the rotating plate. The configuration of this interferometer is the same but, for the proof of concept, the spacing between the π and $^{\pi}/_{2}$ beams is 2mm. A picture of this interferometer is shown in Figure 4-2. To see interferences by this experiment, we have to induce a frequency difference between the π and $^{\pi}/_{2}$ beams of 1kHz. Using the following equation, we can estimate what will the phase shift difference between the reference signal and the interferometer signal:

$$\Delta\phi = \phi_1 - 2\phi_2 + \phi_3 \tag{4.1}$$

With $\phi_i = \vec{k} \cdot \vec{x} - \omega_i t$. We can now express the phase shift without the $\vec{k} \cdot \vec{x}$. Indeed, the difference in phase shift will be due to the $\omega_i t$ which cancels if there is no phase difference between the π and $^{\pi}/_{2}$ beams.

$$\Delta\omega \equiv \omega_2 - \omega_1 = \omega_2 - \omega_3 = 1\ kHz \tag{4.2}$$

So,

$$\Delta\phi = 2\Delta\omega t \tag{4.3}$$

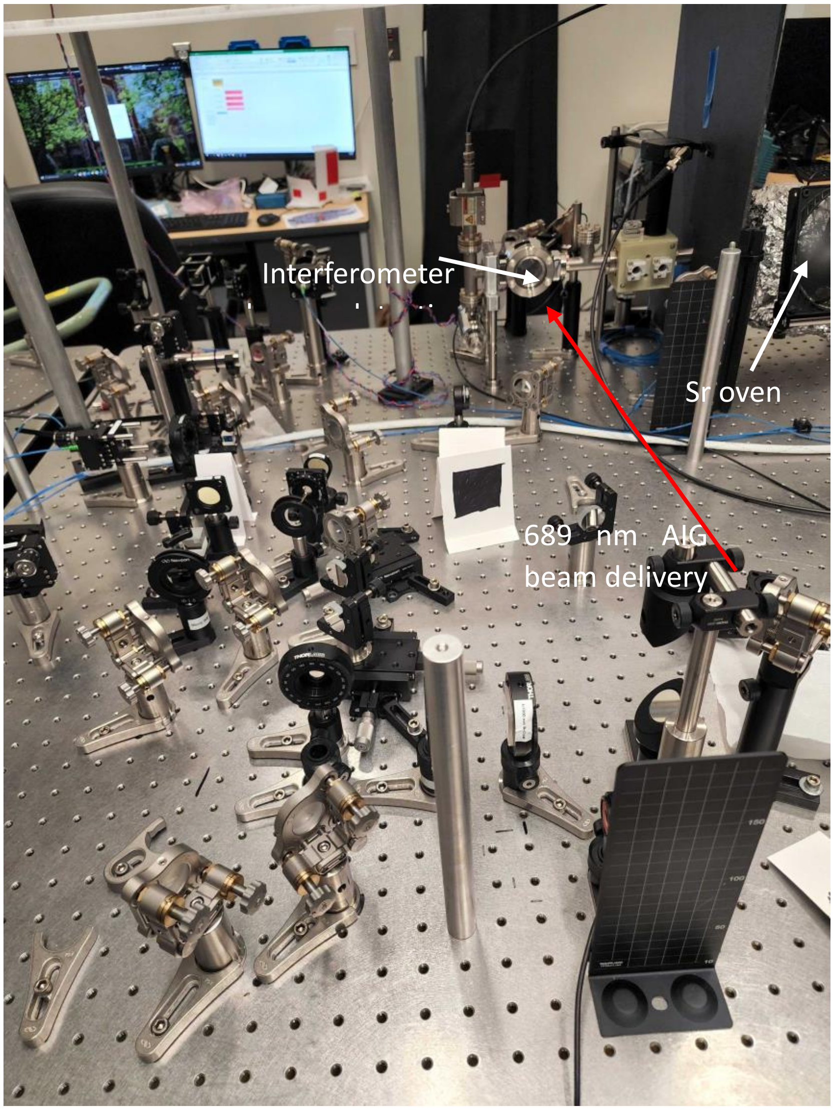

Figure 4-1. Picture of the proof-of-concept interferometer

The result of this interferometer is shown in the next figure. The blue signal is the interferometer signal, and the grey is the reference signal. The signal is clearly in accordance with our theoretical expectation. Moreover, according to the graphic, the interferometer signal has an amplitude of 12 mV.

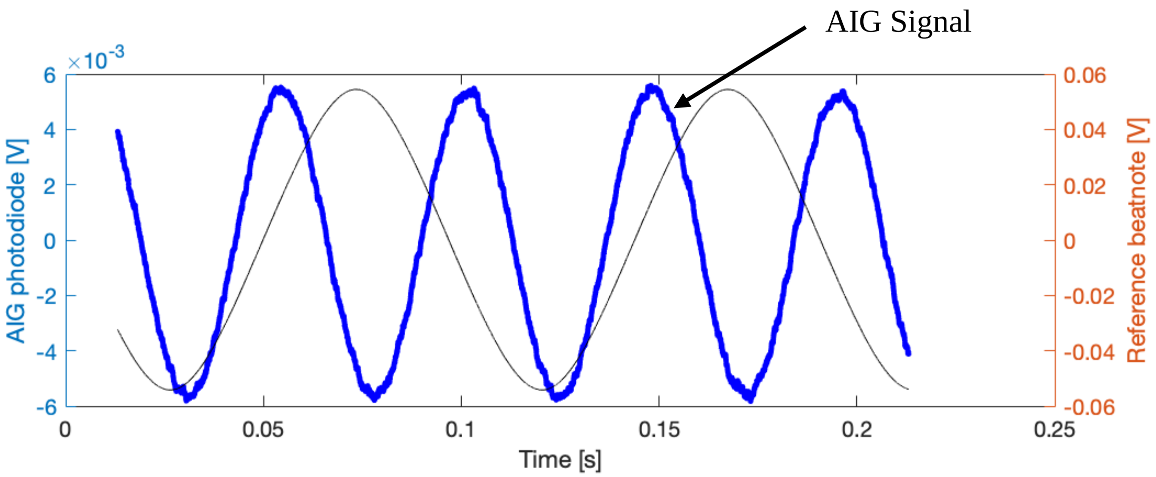

Figure 4-2. Graphic of the proof-of-concept interferometer signal

Using this result, we can now estimate the sensitivity of the rotation rate if this signal was an AIG signal. To estimate this sensitivity, we have to start with the detector design. The detector used is the Hamamatsu described in the precedent chapter. This detector is contained in a box drilled in front of the active region. A half-inch tube is fixed to the box in front of the hole so the active region can detect the fluorescence. Because the active region of the detector is small, we use a 24 mm converging lens that concentrates the light from the fluorescence to the active region. So, the area of the lens can be considered the active region of the detector. A schematic of the tube section is represented in the following figure.

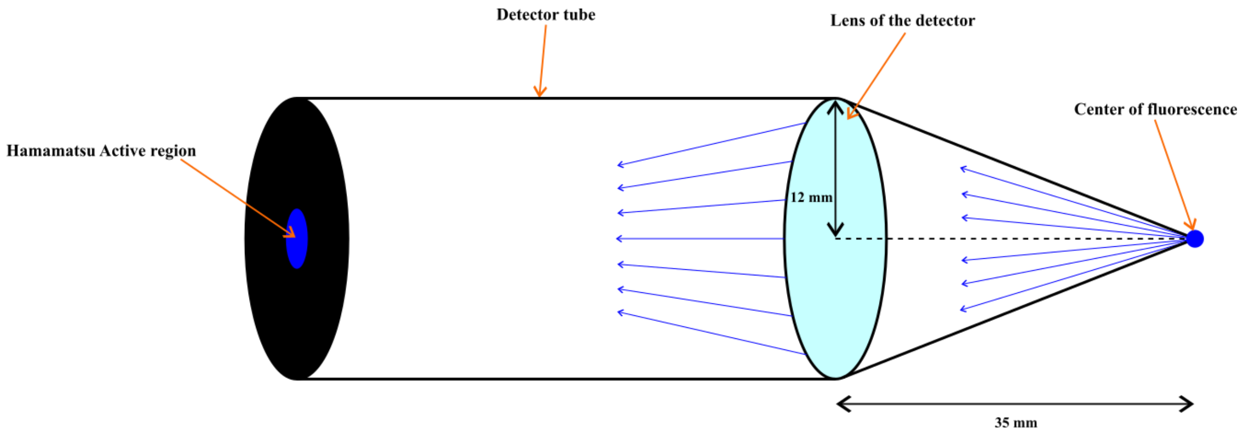

Figure 4-3. Tube section scheme of the AIG detector

Using the solid angle equation, we can calculate the percentage of the total photons released by fluorescence going into the detector χ:

$$\chi = \frac{A_{Lens}}{A_{tot\,sphere}} = \frac{\pi \times 12^2}{4\pi \times 35^2} = 2.94\% \tag{4.4}$$

We can now write the power carried by a single atom during the experiment:

$$P_{atom} = \frac{\Gamma_{1S0\to1P1}}{2} \times E_\gamma = \frac{\Gamma_{1S0\to1P1}}{2} \times \frac{hc}{\lambda_{461}} = 4.33 \times 10^{-11}\ \ W/atom \tag{4.5}$$

At saturation, the scattering rate of the $^1S_0 \to {}^1P_1$ transition is only $^1/_2$, so $\Gamma_{1S0\to1P1}$has to be divided by two. We can now express what will be the signal generated by a single photon using the photosensitivity of the detector:

$$U_{atom} = SP_{atom} = 8.66 \times 10^{-4}\ \ V/atom \tag{4.6}$$

With $S = 2 \times 10^7\ \ V/W$ the photosensitivity of our detector. We know that the amplitude of our AIG signal is $U_{pp} = 12\,mV$, so we can estimate the number of atoms involved in the transition, and producing this signal:

$$U_{tot} = \chi N U_{atom} = 12\,mV \tag{4.7}$$

So,

$$N = \frac{U_{tot}}{U_{atom}\chi} = 471\ atoms \tag{4.8}$$

We can now calculate the atoms' flux in the interferometer's detecting region.

$$\Phi = \rho A\bar{v} = \frac{N}{hA} \times A\bar{v} = \frac{N}{h} \times \bar{v} = 9.94\ \times 10^{7} atoms/s \tag{4.9}$$

Finally, we can express the phase shift as a function of the rotation rate:

$$\Delta\phi = 2k\bar{v}\Omega T^{2} \tag{4.10}$$

With $k = {}^{2\pi}/_{\lambda_{689}}$ is the wavevector of the π and ${}^{\pi}/_{2}$ beams and $T = {}^{L}/_{\bar{v}}$, $L = 7\ mm$. So, we can write the following equation:

$$d\Omega = \frac{\bar{v}\, d\phi}{2kL^{2}} \tag{4.11}$$

With $\mathrm{d}\phi = {}^{1}/_{\sqrt{\Phi}}$, due to atom shot noise[33]. So, after applying equation 4.11 to the flux we found previously, we find a sensitivity for our "AIG" of $\mathrm{d}\Omega = 42.6\ {}^{\frac{\mu rad}{s}}/_{\sqrt{Hz}}$. This result can be enhanced by the transverse cooling that was not working during the signal acquisition. Indeed, the number of atoms involved in the experiment will clearly increase. Furthermore, other sensitivity enhancements are possible and will be discussed in the next section.

CHAPTER 5 - Conclusion

5.1 Summary and current status

In this paper, we have described the design and the functioning of a new Atom Interferometer Gyroscope. The use of the $^1S_0 \rightarrow {}^3P_1$ transition of strontium atom for AIGs has never been experimented. The proof of this concept has been the first experiment done with a part of the apparatus (optical systems and chamber). The result of this experiment is a signal that validates the concept of using strontium atoms in the atom interferometer gyroscope domain. The gyroscope itself has been designed and assembled in the second phase. In the near future, we will test this gyroscope to obtain an AIG signal. The next step will be to hybridize this gyroscope with a Fiber Optic Gyroscope to compensate for the Doppler shift due to the rotation and investigate new possibilities for extending the baseline and enhancing sensitivity.

5.2 Future developments

Even though our apparatus has not been tested yet, we can use the proof of concept, among others, to imagine improvements. A first improvement could be implementing a longitudinal velocity compression with cooling. Indeed, our signal can be improved by increasing the number of atoms involved in the detecting volume at a given time. For this purpose, a cooling system can be achieved on the last axis not cooled yet, the atomic propagation axis. Indeed, the laser beam in charge of this cooling would be counterpropagating compared to the atoms' propagation direction.

Another improvement of our apparatus can be the use of velocity selection. Right now, the velocity used in the calculation is an average done on the velocity spectrum of the atomic beam. However, all the atoms don't propagate exactly at this speed. A velocity selector can reduce the spread of this velocity spectrum and improve the signal by significantly reducing the background in our measurements. Of course, not only the atomic propagation axis can be velocity selected. The transverse velocity selection could also eliminate the atoms diverging too much with respect to the propagation axis. For more theoretical information, see [34], [35]

Our interferometer can be improved in another way. By increasing the baseline, our interferometer could produce a much greater signal. A way to increase this baseline would be to use a Large Momentum Transfer (LMT) interferometer instead of our classical Mach-Zehnder-like Interferometer[36], [37]. As shown in Figure 5-1, the LMT interferometer require multiple pulses. In this case, we could transform our space domain interferometer in a time domain one This figure represents an LMT interferometer using a large number of π beams, but it can be achieved with a small number of added beams. Each time the atomic beam interact with a π-pulse, the atomic momentum is modified and so, multiple well-chosen π-pulses can modify the length and the form of the interferometer as needed.

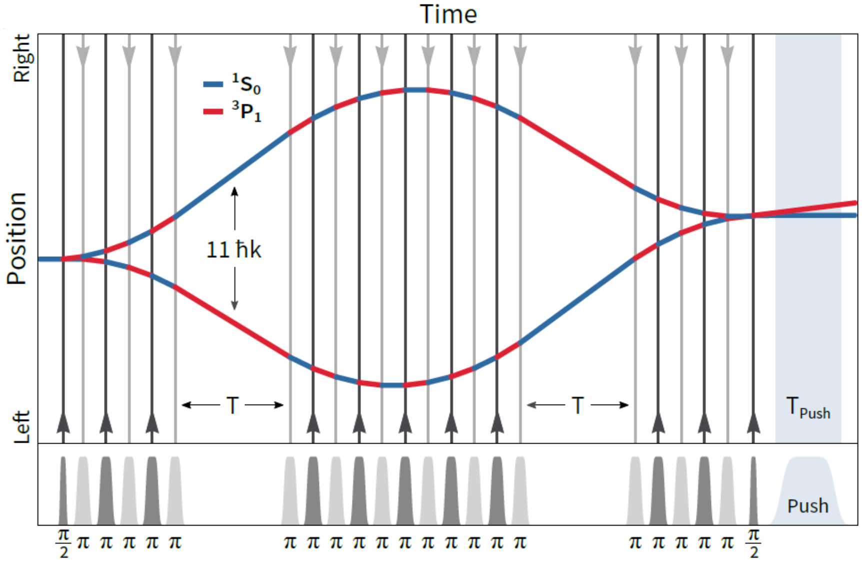

Figure 5-1. Large Momentum Transfer atom interferometry principle.
Figure reproduced from[37].

The particularity of the LMT is that the sensitivity is divided by the number of π-pulses used. For example, using the same signal obtained in the proof of concept but using a LMT and replacing L with one meter and using $N_{\pi-\mathrm{pulse}} = 50$, the sensitivity of our interferometer would be $\mathrm{d}\Omega_{LMT} = \frac{\mathrm{d}\Omega_{Mach-Zehnder}}{N_{\pi-\mathrm{pulse}}} = 0.26\ {}^{\frac{nrad}{s}}\Big/_{\sqrt{Hz}}$, which correspond to a sensitivity 1.5×10^5 times better compared to our expected AIG signal.

REFERENCES

[1] V. M. N. Passaro, A. Cuccovillo, L. Vaiani, M. De Carlo, and C. E. Campanella, “Gyroscope Technology and Applications: A Review in the Industrial Perspective,” *Sensors*, vol. 17, no. 10, Art. no. 10, Oct. 2017, doi: 10.3390/s17102284.

[2] *The Anschutz Gyro-Compass and Gyroscope Engineering*. Watchmaker Publishing, 2003.

[3] J. B. Scarborough, *The Gyroscope. Theory and Applications.*, First Edition. Interscience, 1958.

[4] J. Gorasia, “Fiber Optic Gyroscopes.” 2010. Accessed: Nov. 17, 2022. [Online]. Available: http://www.jgorasia.com/Files/Spring10/Instrumentation/FOGreport.pdf

[5] A. D. V. Di Virgilio, “Sagnac Gyroscopes and the GINGER Project,” *Front. Astron. Space Sci.*, vol. 7, 2020, Accessed: Nov. 17, 2022. [Online]. Available: https://www.frontiersin.org/articles/10.3389/fspas.2020.00049

[6] J. Fang and J. Qin, “Advances in Atomic Gyroscopes: A View from Inertial Navigation Applications,” *Sensors*, vol. 12, no. 5, pp. 6331–6346, May 2012, doi: 10.3390/s120506331.

[7] J. S. Bardi, “Landmarks: Laser Cooling of Atoms,” *Physics*, vol. 21, p. 11, Apr. 2008, doi: 10.1103/PhysRevLett.61.169.

[8] R. Delhuille *et al.*, “Atom interferometry,” *Europhys. News*, vol. 34, no. 4, Art. no. 4, Jul. 2003, doi: 10.1051/epn:2003401.

[9] A. D. King, “Inertial Navigation - Forty Years of Evolution,” *undefined*, 1998, Accessed: Nov. 17, 2022. [Online]. Available: https://www.semanticscholar.org/paper/Inertial-Navigation-Forty-Years-of-Evolution-King/b67513d4d222eee35409b8e03d52ae52bc8346b0

[10] A. Noureldin, T. B. Karamat, and J. Georgy, *Fundamentals of Inertial Navigation, Satellite-based Positioning and their Integration*. Berlin, Heidelberg: Springer Berlin Heidelberg, 2013. doi: 10.1007/978-3-642-30466-8.

[11] T. Nilsson, J. Boehm, and H. Schuh, *Determination of Earth rotation by combining VLBI and ring laser observations*. 2012, pp. 152–155. Accessed: Nov. 17, 2022. [Online]. Available: https://ui.adsabs.harvard.edu/abs/2012jsrs.conf..152N

[12] O. Graydon, “Giant laser gyroscope detects Earth’s wobble,” *Nat. Photonics*, vol. 6, no. 1, Art. no. 1, Jan. 2012, doi: 10.1038/nphoton.2011.332.

[13] K. U. Schreiber, T. Klügel, and G. E. Stedman, “Earth tide and tilt detection by a ring laser gyroscope,” *J. Geophys. Res. Solid Earth*, vol. 108, no. B2, 2003, doi: 10.1029/2001JB000569.

[14] K. U. Schreiber, T. Klügel, J.-P. R. Wells, R. B. Hurst, and A. Gebauer, “How to Detect the Chandler and the Annual Wobble of the Earth with a Large Ring Laser Gyroscope,” *Phys. Rev. Lett.*, vol. 107, no. 17, p. 173904, Oct. 2011, doi: 10.1103/PhysRevLett.107.173904.

[15] K. U. Schreiber, G. E. Stedman, H. Igel, and A. Flaws, “Ring Laser Gyroscopes as Rotation Sensors for Seismic Wave Studies,” in *Earthquake Source Asymmetry, Structural Media and*

Rotation Effects, R. Teisseyre, E. Majewski, and M. Takeo, Eds. Berlin, Heidelberg: Springer, 2006, pp. 377–390. doi: 10.1007/3-540-31337-0_29.

[16] R. P. del Aguila, T. Mazzoni, L. Hu, L. Salvi, G. M. Tino, and N. Poli, "Bragg gravity-gradiometer using the 1S0–3P1 intercombination transition of 88Sr," *New J. Phys.*, vol. 20, no. 4, p. 043002, Apr. 2018, doi: 10.1088/1367-2630/aab088.

[17] K. Y. Khabarova *et al.*, "Spectroscopy of intercombination transition for secondary cooling of strontium atoms," *Quantum Electron.*, vol. 45, no. 2, p. 166, Feb. 2015, doi: 10.1070/QE2015v045n02ABEH015638.

[18] Y. N. Martinez, "Studies of the 5s2 1 S0-5s5p 3P1 transition in atomic strontium," Thesis, Rice University, 2005. Accessed: Nov. 17, 2022. [Online]. Available: https://scholarship.rice.edu/handle/1911/17799

[19] E. C. Cook, L. vers un site externe, and celui-ci s'ouvrira dans une nouvelle fenêtre, "Laser Cooling and Trapping of Neutral Strontium for Spectroscopic Measurements of Casimir-Polder Potentials," Ph.D., Ann Arbor, United States, 2017. Accessed: Nov. 17, 2022. [Online]. Available: https://www.proquest.com/docview/2015157975/abstract/C4EADFA926794A97PQ/1

[20] H. Miyake, N. C. Pisenti, P. K. Elgee, A. Sitaram, and G. K. Campbell, "Isotope-shift spectroscopy of the 1S0 → 3P1 and 1S0 → 3P0 transitions in strontium," *Phys. Rev. Res.*, vol. 1, p. 10.1103/PhysRevResearch.1.033113, 2019, doi: 10.1103/PhysRevResearch.1.033113.

[21] D. Vogel, "Stabilizing a diode laser onto the 1S0 → 3P1 intercombination line of strontium Towards an ultracold strontium experiment," Universidade de São Paulo, São Paulo, 2012.

[22] C. J. Foot, *Atomic Physics*, 1st edition. Oxford ; New York: Oxford University Press, 2005.

[23] C. Cohen-Tannoudji and D. Guéry-Odelin, *Advances in Atomic Physics: An Overview*. WORLD SCIENTIFIC, 2011. doi: 10.1142/6631.

[24] G. Nemova, *Field Guide to Laser Cooling Methods*. SPIE, 2019. doi: 10.1117/3.2538938.

[25] M. M. Boyd, "High precision spectroscopy of strontium in an optical lattice: Towards a new standard for frequency and time," 2007. Accessed: Nov. 17, 2022. [Online]. Available: https://ui.adsabs.harvard.edu/abs/2007PhDT.......201B

[26] C. Overstreet, P. Asenbaum, and M. A. Kasevich, "Physically significant phase shifts in matter-wave interferometry," *Am. J. Phys.*, vol. 89, no. 3, pp. 324–332, Mar. 2021, doi: 10.1119/10.0002638.

[27] F. A. Narducci, A. T. Black, and J. H. Burke, "Advances toward fieldable atom interferometers," *Adv. Phys. X*, vol. 7, no. 1, p. 1946426, Dec. 2022, doi: 10.1080/23746149.2021.1946426.

[28] K. Bongs, R. Launay, and M. A. Kasevich, "High-order inertial phase shifts for time-domain atom interferometers," *Appl. Phys. B*, vol. 84, no. 4, pp. 599–602, Sep. 2006, doi: 10.1007/s00340-006-2397-5.

[29] S. Abend *et al.*, "Atom interferometry and its applications," Jan. 2020. Accessed: Nov. 17, 2022. [Online]. Available: https://ui.adsabs.harvard.edu/abs/2020arXiv200110976A

[30] T. Gustavson, A. Landragin, and M. Kasevich, “Rotation Sensing with a Dual Atom-Interferometer Sagnac Gyroscope,” *Class. Quantum Gravity*, vol. 17, p. 2385, Jun. 2000, doi: 10.1088/0264-9381/17/12/311.

[31] E. D. Black, “An introduction to Pound–Drever–Hall laser frequency stabilization,” *Am. J. Phys.*, vol. 69, no. 1, pp. 79–87, Jan. 2001, doi: 10.1119/1.1286663.

[32] R. Senaratne, S. V. Rajagopal, Z. A. Geiger, K. M. Fujiwara, V. Lebedev, and D. M. Weld, “Effusive atomic oven nozzle design using an aligned microcapillary array,” *Rev. Sci. Instrum.*, vol. 86, no. 2, p. 023105, Feb. 2015, doi: 10.1063/1.4907401.

[33] W. M. Itano *et al.*, “Quantum projection noise: Population fluctuations in two-level systems,” *Phys. Rev. A*, vol. 47, no. 5, pp. 3554–3570, May 1993, doi: 10.1103/PhysRevA.47.3554.

[34] D. Kosachiov and Y. Rozhdestvensky, “Raman velocity selection of a three-level atom in a modulated light field,” *Quantum Semiclassical Opt. J. Eur. Opt. Soc. Part B*, vol. 8, no. 3, p. 599, Jun. 1996, doi: 10.1088/1355-5111/8/3/021.

[35] A. I. Pegarkov, “Spectra of resonance raman scattering during slow atomic collisions in intense laser field,” in *Proceedings of 5th European Quantum Electronics Conference*, Amsterdam, Netherlands, 1994, pp. 56–57. doi: 10.1109/EQEC.1994.698123.

[36] T. Mazzoni, X. Zhang, R. Del Aguila, L. Salvi, N. Poli, and G. M. Tino, “Large-momentum-transfer Bragg interferometer with strontium atoms,” *Phys. Rev. A*, vol. 92, no. 5, p. 053619, Nov. 2015, doi: 10.1103/PhysRevA.92.053619.

[37] J. Rudolph *et al.*, “Large Momentum Transfer Clock Atom Interferometry on the 689 nm Intercombination Line of Strontium,” *Phys. Rev. Lett.*, vol. 124, no. 8, p. 083604, Feb. 2020, doi: 10.1103/PhysRevLett.124.083604.